Fall 11-17-2018

Metal Segregation During the Solidification of Titanium-Aluminum Alloys for 3D Printing Applications

Jwala Parajuli

Recommended Citation

Parajuli, Jwala, "" (2018). *Thesis*. 6.
https://digitalcommons.latech.edu/theses/6

METAL SEGREGATION DURING THE SOLIDIFICATION OF TITANIUM-ALUMINUM ALLOYS FOR 3D PRINTING APPLICATIONS

by

Jwala Parajuli, BS Nanosystems Engineering

A Thesis Presented in Partial Fulfillment
of the Requirements of the Degree
Master of Science

COLLEGE OF ENGINEERING AND SCIENCE
LOUISIANA TECH UNIVERSITY

November 2018

LOUISIANA TECH UNIVERSITY

THE GRADUATE SCHOOL

SEPTEMBER 28, 2018
Date

We hereby recommend that the thesis prepared under our supervision by

Jwala Parajuli, BS Nanosystems Engineering

entitled **Segregation during the Solidification of Ti-Al Alloys for 3D Printing Applications**

be accepted in partial fulfillment of the requirements for the Degree of

Master of Science in Molecular Science and Nanotechnology

Supervisor of Thesis Research

Head of Department

Molecular Science and Nanotechnology
Department

Recommendation concurred in:

Advisory Committee

Approved:

Director of Graduate Studies

Dean of the College

Approved:

Dean of the Graduate School

GS Form 13
(8/10)

ABSTRACT

Titanium-Aluminum alloys are one of the widely used alloys in multiple engineering applications. They are highly preferred in Selective Laser Melting (SLM) processes due to their low density, high melting temperature, and good strength. Segregation occurs during the solidification of most alloys and produces a non-uniform distribution of atoms. In SLM, segregation may depict the type of adhesion between the two deposited interfacial layers and the strength between the interphase between an already solidified layer and a new one, and overall, the quality of the printed part. In order to avoid segregation, the understanding of the segregation behavior at atomistic level is important. The main goal of this work is to understand the metal segregation in titanium-aluminum alloys for 3D printing applications using molecular simulations. For this the solidification of metal alloys is computationally simulated and the atomic ordering and structural transformations of the systems are studied. The thermal stability of different compositions of titanium-aluminum metal alloys and the size effects of the system on atomic ordering, structural transformation, and thermal stabilization of the alloys using Molecular Dynamics (MD) simulations is done. MD simulations are widely used in the studies of atomic transformations and structural evolutions of molecular systems and require the use of forcefields to describe the forces between atoms. In addition to the main goal, in this the performance of the Zope-Mishin Embedded Atom Method (EAM) and the Sun-Ramachandranan-Wick Modified Embedded Atom Method

(MEAM) potential developed for the titanium-aluminum systems is evaluated. This work is divided into two parts. In the first part, the simulations are carried out in nine different compositions of 3.4 nm titanium-aluminum spherical nanoclusters with the timestep of 2 fs, the equilibration time of 50 ps, and the total simulation time of 2 ns and in the second part the simulations are carried out in two titanium-rich clusters of the same composition but different sizes are done at the timestep of 1 fs, the equilibration time of 100 ps, and the total simulation time of 1 ns. Each study is done twice using two different forcefields each time. The clusters are melted at high temperature and solidified at room temperature (300K) using simulated annealing. The analysis is done using the radial density distribution of atoms, the structural evolutions from the trajectories, and the melting temperature calculations using the combination of caloric and heat capacity curves using both forcefields. From the EAM potential, the solidified titanium-rich clusters show an inclination to icosahedral geometry whereas the MEAM potential shows the solidified aluminum-rich clusters to have an inclination to truncated octahedral geometry. Moreover, MEAM calculated the melting temperature of pure aluminum nanocluster at 711.76K and pure titanium nanocluster at 1185.36K. In the clusters except for the ones with high titanium concentration, aluminum migrates to the surface upon solidification. Due to the presence of titanium in the grain boundary making the adhesion between two SLM interfacial layers stronger. These high titanium clusters are found to have low segregation and suggested in SLM printing applications. The size effect study done shows no significant change in the properties of the structures or the melting temperatures.

APPROVAL FOR SCHOLARLY DISSEMINATION

The author grants to the Prescott Memorial Library of Louisiana Tech University the right to reproduce, by appropriate methods, upon request, any or all portions of this Thesis. It is understood that "proper request" consists of the agreement, on the part of the requesting party, that said reproduction is for his personal use and that subsequent reproduction will not occur without written approval of the author of this Thesis. Further, any portions of the Thesis used in books, papers, and other works must be appropriately referenced to this Thesis.

Finally, the author of this Thesis reserves the right to publish freely, in the literature, at any time, any or all portions of this Thesis.

Author ______________________________

Date ______________________________

GS Form 14
(8/10)

DEDICATION

To my greatest pillar of strength and my motivator for life, my husband Dr. Suraj Gyawali and my dearest parents who brought me to this world and made me worthy of this accomplishment.

Thank you for your unconditional love.

TABLE OF CONTENTS

LIST OF FIGURES

LIST OF TABLES

ACKNOWLEDGMENTS

I would like to acknowledge the financial support of the Consortium for Innovation in Manufacturing and Materials (CIMM) National Science Foundation EPSCoR Research Infrastructure Improvement (RII) Track -1 Award for Louisiana, whose support helped me with the resources needed for this study.

A huge thank you to Dr. Daniela Mainardi, the advisor for my graduate studies, for mentoring me throughout this research and helping me gain the understanding and knowledge required to get this work done. Your guidance and support have helped me become a better version of me.

Thank you Dr. Ramu Ramachandranan, the member of my advising committee, for always being there for everything I have needed. Your compassion has helped me become a confident person.

My sincere thank you to Dr. Pedro Derosa, the member of my advising committee, for helping me have the visual clarity of the big picture that this research is aimed at.

Thank you, Dr. Collin Wick, the Associate Dean Interim of the COES for always welcoming me to your office to help me with my research and giving me a perspective.

My husband, Suraj Gyawali, thank you very much for being the best guide. Without your motivation I would never be able to explore the hidden researcher in me. You have made me a better thinker and a better researcher.

Thank you very much my father Janaki Prasad Parajuli, my mother Rachana Parajuli, my other father, Govinda Gyawali, and my other mother, Rama Gyawali, my sisters, Jyotsaana Parajuli and Jasmine Parajuli, and my brothers, Sumit Gyawali, and Pratik KC for always being there for me and loving and supporting me in everything I do. Your love and support have always encouraged me to do better.

CHAPTER 1

BACKGROUND

1.1 Additive Manufacturing

Additive Manufacturing (AM) is an alternate to rapid prototyping methods. Unlike the rapid prototyping methods that have been used to produce prototypes for visual testing and fit evaluation, AM process is focused on the creation of functional shaped parts. The production of parts additively, layer by layer, was first described and patented in the 1980s [1] by groups in several countries, including Japan, France and the USA. Several different approaches to rapid prototyping and additive manufacturing have since been developed. AM involves the production of parts layer by layer, with each layer forming a cross section of the part. To form a layer, the powder feedstock is melted and solidified. Another layer of the material is formed by depositing the material in the previous layer and fused together. AM is capable of fabricating complex integrated parts, therefore making it one of the most researched manufacturing methods [2]. AM processes are mostly laser based because the high intensity and highly assimilated beam of energy produced by a laser can create dense parts for high stress applications [1]. AM can be classified into seven categories based on the type of process they use namely, vat polymerization, material jetting, material extrusion, sheet lamination, binder jetting, directed energy deposition, and powder bed fusion [3].

1.1.1 Vat Polymerization

Vat polymerization [3] uses plastics and polymers as the raw feed and involves the selective curing of liquid polymers in a vat by ultraviolet light. After a layer has been created, it is re-coated with polymer resin and the process is repeated. The first vat polymerization system was the Stereolithography Apparatus (SLA) patented by Charles Hull in 1984 [4] and marketed by 3D systems. This was also the first commercial, additive, free-form fabrication process. In SLA, the photopolymer is cured by the means of 17 galvanically steered laser spots. Modern developments include the use of micro mirror arrays (Digital Light Processing (DLP) technology) [5] [6] to project light patterns [5], micro scale lithography [7] and more sophisticated resins [8] [9].

1.1.2 Material Jetting

In material jetting processes, droplets of material are sprayed from a nozzle (or series of nozzles) in order to build up layers. The jetting may be achieved by piezoelectric, thermal or by jetting in an aerosol form [10] [11]. Materials can include polymers and photopolymers, waxes, ceramics [12] and metals [1] [5] [13]. If a photopolymer is employed, an appropriate light source adjacent to the deposition head is used as a source of energy for curing. The first such devices were manufactured and marketed by Solidscape Inc. in 1994 [1]. More recently, this method has been extended to the direct production of functionally graded and multi-material parts, electronic components that include both conductive and insulating elements [14] and weld-based production of metal parts using droplets of molten metal [15] [16] .

1.1.3 Material Extrusion

Material extrusion processes are among the most common solid free-form fabrication systems in use today, representing the largest installed base [17]. In material extrusion processes a continuous stream of material extruded from a nozzle is used to build up part layers. The nozzle is moved relative to the build platform, in order to create the layer geometry. The first material extrusion system, Fused Deposition Modeling (FDM) was developed and patented by Scott Crump in 1989 [18]. FDM systems produce thermoplastic parts by the extrusion of a stream of material heated to above its glass transition temperature. Materials include a wide variety of engineering plastics such as Nylon, Acrylonitrile Butadiene Styrene (ABS), Polyactic Acid (PLA), and Polycarbonate [19]. Other materials that may be processed by FDM style material extrusion include metals [20] and ceramics [21] [22] by powder filled filament as well as composite material by filament containing reinforcing 19 fibers. Systems capable of extruding cement and high-performance concrete, bio-compatible materials, food [23], and conductive elements [24] have also been developed.

1.1.4 Sheet Lamination

Sheet lamination processes produce parts by fusing sheets of material one on top of the other, forming a laminate. The cross section of the part is cut out of each sheet either after bonding or before bonding [1] [5]. After production, the sections of the laminate not corresponding to the part are broken off. The process of removing excess material may be assisted by the addition of a hatch pattern in the excess material while the layer profile is also being created. The first sheet lamination process, Laminated Object Manufacturing (LOM) can be credited to Michael Feygin and Helisys Inc. in

1985-86 [25]. Sheets may be composed of metal, polymer, or paper. Cross sections may be created by cutting with lasers or by mechanical means such as Computer Numerical Controlled (CNC) milling or cutting multiple sheets with a blade. Bonding may be achieved chemically, thermally or by ultrasonic welding.

1.1.5 Binder Jetting

In Binder Jetting processes, layers are generated by selectively spraying a binder onto a powder bed. The binder fuses the powder to form a solid layer. Once a layer is created, the powder bed is lowered, re-coated with an even layer of powder and the process is repeated to build up the object. The first binder jetting processes was '3D printing', developed at MIT in 1989 [26]. Modern Binder Jetting processes can be used to create plastics, composites, ceramic, sand [27] [28] and metal parts [29]. This process is also capable of generating full color parts, by using pigments along with the binder. Curing, infiltration and sintering may be required after initial part production for the part to achieve its final strength and surface characteristics [30].

1.1.6 Directed Energy Deposition

Directed energy deposition processes are similar to material jetting and material extrusion is some respects. In directed energy deposition systems, focused thermal energy is used to bond materials to the substrate in order to build up layers. The material may consist of a continuous wire feed or powder carried by an inert gas [31]. The thermal energy may be supplied by laser [32], electron beam [33], or plasma arc [34] . The first powder based directed energy deposition systems was the Laser Engineered Net Shaping (LENS) process developed at Sandia Labs and marketed by Optomec [1]. These systems are primarily used to produce metal parts, including high performance aerospace alloys

[35], and are often used for mold and part repair and re-manufacture. Materials can include functionally graded parts produced by varying the material composition during the building process.

1.1.7 Powder Bed Fusion

Powder Bed Fusion processes function similarly to binder jetting in that solid layers are generated by fusing powder together, in a powder bed. In powder bed fusion, however, the binding is achieved by the application of thermal energy (in the form of focused energy) rather than chemical energy. The first process of this type was Selective Laser Sintering (SLS) developed in the late 1980s by Joseph Beaman and Carl Deckard and marketed by the DTM Corporation [36]. In SLS, the powder material is partially melted by focused CO_2 laser beam. The structural material remains solid whereas the binder material gets melted. SLS uses galvano mirrors as a beam deflection system and can use plastics, metals, polymer, and ceramics as raw materials. The layers are bind together usually by a polymer binder which is later removed by heating [37]. SLS can be classified into Solid State Sintering, Chemically Induced Binding, and Liquid-Phase Sintering Partial Melting depending on the binding mechanism. The thermal energy may cause either sintering as in SLS or complete melting as in Selective Laser Melting (SLM). SLM is similar to SLS except the powder material is fully melted in SLM creating a much denser product than SLS [38] [39]. Super alloys, aluminum, stainless steel, tool steel, cobalt chromium, and titanium are among the most used SLM raw materials [40]. Powder bed fusion can be used to generate thermoplastics, ceramics and metals as well as composite materials. Lasers, focused light and Electron Beams have been used as energy sources.

Our research work focuses on the SLM process and the defects in the SLM printed parts. Therefore, we will further discuss in detail about the SLM process in the next section.

1.2 Selective Laser Melting

SLM is the most successful and promising of all the AM techniques and is used widely to fabricate metal parts. SLM uses a high-power laser heat source that sweeps a defined area of powder metal (pure/alloy) for the creation of the 3D part in successive layers. As the beam passes through the powder, a melt pool is formed which solidifies as the beam continues its sweeping. The schematics of SLM process can be seen in **Figure 1-1.**

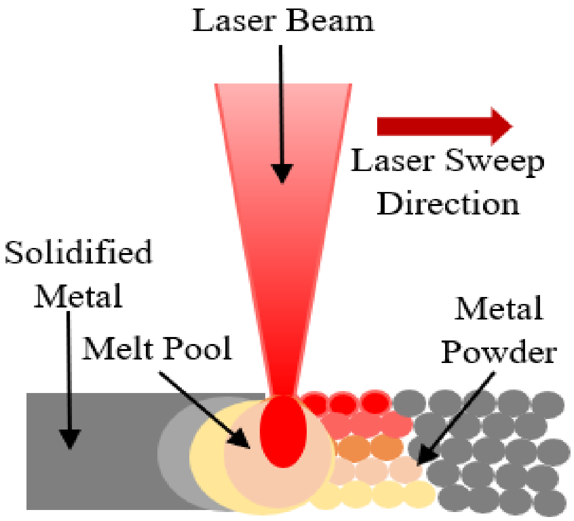

Figure 1-1: The schematics of the selective laser melting process

SLM can be used to create parts with hollow structures and graded porosity, therefore the process has almost infinite geometrical freedom [39]. The advantages of SLM are that there is low materials waste, no need for mold, the production time is low with a few production steps, can work with materials with high melting points, and the process is highly flexible (designs can be altered). However, there are some defect-related issues in SLM that needs to be studied and corrected so that the printed parts are defect free and of high quality [41] [42] [43].

The main parameters that have impact on the quality of the final product in SLM are the laser power, scan speed, hatch spacing, and the layer thickness. High laser power may result in material evaporation whereas low laser power may result in balling. Porosity and surface roughness are caused by poor hatch spacing and large layer thickness ultimately causing balling [44] [45] . Heat conduction is rapid in the areas away from the melt pool. This causes significant amount of laser energy to be consumed. Apparently, the increase in laser energy causes the melt pool to be larger and drags unmelted powder metal into it [46]. This is one of the reasons for surface roughness in printed parts. Understanding the solidification process of the interfacial layers is equally important since it controls the adhesion and strength of the printed parts.

Besides the parameters mentioned above, there are a few other manufacturing and post processing steps that are being mostly researched to print defect-free parts of high quality. We will address them as the “Challenges in SLM” in the next chapter.

CHAPTER 2

INTRODUCTION

2.1 Challenges in Selecting Laser Melting

Even though SLM has been a promising and a breakthrough technology, there are some challenges that have caused it to have commercial setbacks. The dynamics of melt pool coalescence, evolution of microstructure and grain growth during re-solidification, residual stress, powder feedstock contamination, and segregation are some of the areas that require more understanding to get a defect free printed part using SLM. These challenges are discussed in detail in this chapter.

2.1.1 Powder Synthesis

Metal powders for SLM can be pure or alloyed. Most common metal powders used in SLM include stainless steels, aluminum, nickel, cobalt-chrome, and titanium alloys. Several studies [47] [48] [49] have reported significant properties (low density, high melting temperature, and high strength) that has helped focus on titanium alloys for 3D metal printing, specifically, titanium-aluminum (Ti-Al) alloys. However, the results varied depending on the alloy composition. Ti-Al alloy powders are widely researched for their use in SLM as they have low density (4.43 g/cm^3 for Ti-6Al-4V) [50], high melting temperature (1878K for Ti-6Al-4V), and good strength (862-1200 MPa of tensile strength for Ti-6Al-4V) [50] [51] [52] making it preferred in aerospace, marine, and other areas [53] where light materials with good strength are required. For metal powders, the shape of the powder grain, the surface condition, cooling rate, and size distribution depends on the powder production process and they define the properties of the final product [54]. The preferred geometry of the powder material for SLM is spherical and is mass produced by atomization. The various atomization methods are gas atomization, water atomization, plasma atomization, and centrifugal atomization. Gas atomization is the most popular method [55] for metal powder synthesis. In gas atomization, metal powders are produced by melting the metal in vacuum and converting the melted metal into fine powders by dispersing the melted droplets in the presence of high pressure in an inert gas. The liquid droplet solidifies and forms fine, spherical, homogenous powders [56]. Water atomization is similar to gas atomization except the atomizing medium is a stream of water. The high cooling rate in water atomization causes rapid solidification of the melted metal/alloys. Therefore, the powders obtained through water atomization have irregular geometry [57]. The feed for plasma atomization is metal wire. Plasma atomization can produce fine powders with the particle size distribution of 0-200 μm with spherical shape [58]. The atomizing medium in plasma atomization is argon plasma. The centrifugal atomization uses centrifugal forces to disperse melted metal which solidifies to form powders. The size distribution of the powder obtained through centrifugal atomization is 50-150 μm [59].

The challenge associated with powder synthesis is achieving controlled powder size with uniformity and purity. Despite being less expensive than other production methods, the limitations in purity associated with oxidation and irregularities in geometry caused by the high impact energy of water [60] on the produced powder makes water atomization unfavorable for SLM powder synthesis. For plasma atomization the initial material needs to be flexible for it to get in the wire feedstock. This limits the raw materials for plasma atomization. Even though the centrifugal atomization generates more spherical powders and is a cheaper powder production method, the limitation is associated with the production of less reactive and low melting point alloys. Therefore, gas atomization is the only technique that is popular for mass production of a wide range of powder metals for SLM. However, the main concern with gas atomization is the large particle size distribution which makes only a fraction of the produced powder usable [61]. To overcome these issues, many researchers have proposed improved and alternate techniques for enhanced powder production. Dietrich *et al.* [62] proposed thermal spraying as an alternate to gas atomization. It was concluded that thermal spraying into an inert gas atmosphere yielded higher powder quality without the worry of chemical reaction with the melted particles. Uhlenwinkel *et al.* [61] have reported that the modification in the gas nozzle (exit angle and diameter) generates smaller particles size and protects the metal from oxidation. They have also reported that an added swirl jet pressure nozzle and a gas nozzle produced tin powders with larger median particle diameter of 15µm. More results are reported everyday however, the commercial viability of these new techniques is still being analyzed.

2.1.2 Grain Growth

Grain growth occurs during the post-processing heat treatment. It is caused by the reduction in interfacial energy [63] [64] [65] between the two created interfacial layers caused by the high cooling rates experienced by the layers being deposited. The melt pool cools down and vertical heat loss causes columnar grains to grow. Chlebus *et al.* [64] reported that the length of laser scan vector which is measured by the back and forth scan pattern and the number of applied layers significantly affect the size of columnar grain growth. Columnar grains are the long thin grains that form when the metal solidifies. The thermal treatment of the material to modify the microstructure was suggested to decrease the defects caused by grain growth. Another experiment was conducted by Krakhmalev *et al.* [66] to study the microstructure formation in Ti-6Al-4V produced by SLM. They concluded that the pore coalescence caused the materials to be ductile with crack formations. They suggest stress relieving heat treatment of the material to improve its mechanical properties by significantly reducing porosity. The grain growth related defects are a big concern in SLM and the ability to manufacture parts from SLM with controlled microstructure is still being researched.

2.1.3 Residual Stress

Materials suffer from residual stress during processing. Residual stress can cause cracks and delamination which reduces the mechanical strength of the product. Patterson *et al.* [67] point out the main cause for residual stress to be heat cycling. Heat cycling involves continuous melting, re-melting, and solidification of powder during the process causing inconsistent heat levels within the environment. Stress gradients and thermal deformation caused by heating and cooling can be seen in **Figure 2-1.**

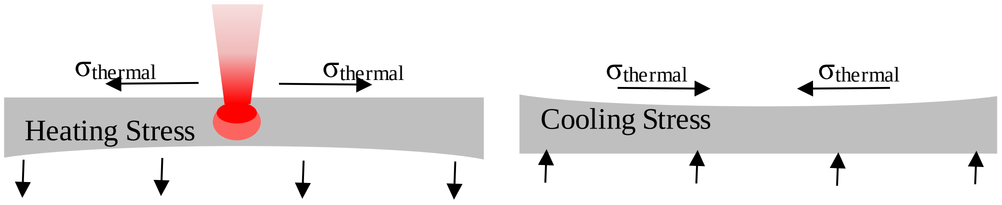

Figure 2-1: The stress gradients in layers caused by heating and cooling [67]

The layers that underlie do not let thermal expansion or compression to further take place. This causes elastic compressive strain in the layers forming stress gradients [68]. Residual stresses in simple designs were reduced by fusing the first powder layer to the base plate. However, the same cannot be helpful in protruding and complex designs. Protrudes are physically not welded to the base plate and are thinner, therefore, they are less resistant to thermal trembling. This decreases the strength of the printed part. Not a lot of work has been successfully done to reduce residual stress in the designs with protruding features however, some researchers have suggested that the use of stronger base material might help in simple designs.

2.1.4 Dynamics of Melt Pool

A melt pool is formed when a high-energy laser hits the powder surface. The expanding melt pool drags unmelted powder on its surroundings along due to its surface tension. The deposition of unmelted powder on the melted metal causes surface roughness in the printed parts. Surface tension of the melt pool depends on the size and aspect ratio of the melt pool [69], therefore, a better understanding of the dynamics of the melt pool will help enhance to address this matter. Many experimental and computational approaches including the Finite Element Method (FEM) have been implemented to model the melt pool in SLM [70] [71] [72]. For the computational part, Gaussian model for laser heat source has been used. The parameters such as hatching distance, scanning speed, absorption rate, laser beam diameter, and laser power are adopted from experimental data. Meshing in most of the studies [72] are uniform with the grid size larger than the beam diameter. The finer meshes are better in computational studies to record the smallest change. However, finer mesh means more computational cost. Few researchers have tried the non-uniform meshing to represent the heat affected zones in their studies [70] [71], but the limitations to these was that the representation was in 2D and the continuous temperature evolution was not considered. Kai *et al.* [73] have used a dynamic meshing technique in their study instead of a steady mesh. They were able to simulate the temperature evolution with time and the thermal distribution by moving the mesh dynamically as the laser scans. They found that the thermal contours at low temperatures are found to be asymmetric while the geometry of the melt pool at the initial scan position, where there is maximum heat, is circular. They have concluded that a much better modeling and simulation tool than ANSYS would be able to do intricate computations in a high energy input problem. This conclusion again leaves room for improvement and more research for better understanding of the melt pool dynamics in SLM.

2.1.5 Powder Feedstock Contamination

Feedstock degradation is one of the challenges SLM faces. Contamination is one of the reasons for the degradation of the powder feedstock and it can alter the chemical composition of the feedstock. Contamination may happen during raw material production, storage, atmospheric interaction, or because of cross-contamination. Beals *et al.* [74] published a patent on improving the SLM process by addressing the atmospheric/moisture contamination. They report that the rapid melting and solidification causes the contaminant to evolve creating bubbles and pores in the material. Their patented product adds a second material to the first material to form a modified powder with two different compositions. The outer surface materials are selected from one of the low moisture/contamination groups of metals (Ti, Zr, Mo, Cr, Mn, Si, Sn, Zn, Pb, Co, and Ni). The outer surface gets dissolved into the melt pool and gets mixed with the interior composition. They concluded that this takes care of the atmospheric/moisture contamination on the powder feedstock that affects the final product. Researchers also have found that cross-contamination of the feed material during the manufacturing process is one of the under addressed causes of feedstock degradation. Brandao *et al.* [75] report that cross-contamination is the most likely source of feedstock degradation. They contacted one of the suppliers of powder feedstock and found out that their tungsten specimen was manufactured on the same machine prior to the Ti-6Al-4V batch. During the SEM and X-ray imaging they were able to find traces of tungsten in the Ti-6Al-4V powder. They concluded that a few vertical specimens built in vertical building direction had lower yield and strength values than those set as the minimum requirements for additive manufacturing printed parts. Other specimens showed above minimum yield and tensile strength values. They concluded that the impact of feedstock contamination on the mechanical properties of products still requires extensive study.

The solutions to these challenges are important to find. To understand the SLM process (melting and solidification), both experimental and computational studies are important. This study will focus on the computational study of metal powders (titanium-aluminum) to explore their structural properties and segregation behavior as a function of time using multi-scale computational tools. This study will help elucidate the metal composition to be used for optimum printed product quality in SLM processes.

2.1.6 Segregation

SLM processes possess a huge challenge associated with segregation effects in the alloyed feedstocks. Alloys with low segregation is preferred in SLM because segregation effects cause inhomogeneity and has damaging effect in the compositional uniformity of the parts fabricated by SLM. Segregation (that is promoted by thermal effects) also alters the adhesion and friction behavior weakening the interface [76]. The atomic ordering in nanoparticles and nanoalloy clusters depend on relative atomic sizes, relative bond strengths, and surface energies of the bulk elements. If the bond between two different atoms is stronger than the bond between two of the same atoms, segregation occurs. In SLM printed parts, segregation to grain boundaries have been evidenced. Kruth *et al.* [77] have reported that the grain boundary segregation may cause a catastrophic loss of ductility in SLM produced parts. In the study done by Bartlomiej *et al.* [78] on Ti-6Al-4V powders, it was found that aluminum segregated to the melt pool boundary because of rapid solidification. They also suggested that the segregation is independent of the powder size and the thickness of the powder layer. However, according to Gorsse *et al.* [43] the segregation of heavy alloying element has been known to have caused dislocation and associated residual stress.

This study focusses in titanium-aluminum binary systems in which case titanium is the heavier alloying element. Since there are limited studies on the segregation effects in SLM [79] [80], this work will focus on the melt pool dynamics and metal segregation. Therefore, this work will try to shed some light on the segregation phenomena that occurs from the melting to the solidification of titanium-aluminum alloys of various concentrations.

2.2 Computational Works in the Area of this Thesis

Several molecular dynamics studies on titanium-aluminum systems have been conducted to understand the transformations and the process of SLM solidification at the atomic level. During melting and solidification, the metals/alloys undergo repeated solid-liquid phase transformations induced by repeated thermal cycles, therefore, it is obvious to expect the influence of these processes in microstructure of the deposited material. The nanocrystallization of metals/alloys increases the corrosion resistance of the material [81]. Pei *et al.* [51] conducted a molecular dynamics study of Ti_3Al alloy (6000 titanium and 2000 aluminum atoms) with Zope-Mishin EAM potential and studied crystallization under different cooling rates. They concluded that Ti_3Al has a relatively weak ability to fully crystallize compared to other titanium-aluminum compositions. However, Xie *et al.* [82] concluded that the crystallization depends on the cooling rate and they were able to fully crystallize Ti_3Al at the cooling rate of 10^{11} K/s. Peng *et al.* [83] conducted molecular dynamics research to study the microstructural changes during solidification. They found that faster cooling rates caused slower atomic migration and formed amorphous structures. But at slower cooling rate the atomic arrangement was orderly with atoms because they had enough time to diffuse. They also concluded that cooling rates play an important role in microstructural changes that affect the properties of the printed material. Another phase transformation study on titanium-aluminum system was done by Zhang *et al.* [52] who found that nucleation depends on the composition of the material. In their study, nucleation in $Ti_{10}Al$ (49090 titanium and 4910 aluminum atoms) occurred earlier than Ti_5Al (46286 titanium and 7714 aluminum atoms) causing stacking faults.

In molecular dynamics, the selection of the forcefield is equally important to describe the interatomic interaction between the atoms. The titanium-aluminum systems have been computationally studied in both solid [84] [85] and liquid state [86]. Lopis *et al.* [87] did a comparative study of EAM potentials developed by Shimono *et al.* [86] and Zope *et al.* [88] on titanium-aluminum system. They reported that the Zope-Mishin EAM produced significantly better values for density, heat capacity, and thermal expansion coefficient. The Shimono EAM potential is based solely on physical measurement whereas the Zope-Mishin EAM potential is developed using the physical and quantum mechanical data. Most of the computational studies [51] [52] have utilized Zope-Mishin interatomic potential developed for titanium-aluminum systems. On the other hand, Hennig *et al.* [89] described that the classical modified embedded atom method potential is better for phase change studies of metal alloys.

2.3 Problem Statement and Objectives of this Work

Study of the structural transformations, atomic ordering, and the thermal stability of the metal systems during solidification is important to improve the SLM process. The atomistic level understanding of the interfacial behavior of the printed layers at various thermal conditions will help identify the parameters that may influence the formation of grains, micro-structural bonding, microporosity, and lack of fusion [90]. This will further dictate the type of adhesion and the final quality and the strength of the interface between the layers already solidified and the new layer being formed during the printing process. Therefore, the goal of this study is to understand the metal segregation behavior in titanium-aluminum alloys in order to identify the alloys that would alter the adhesion for

3D printing applications using molecular simulations. This goal is accomplished by the following objectives;

a) To elucidate atomic ordering and distribution in the alloys during solidification using molecular simulations.
b) To study the structural transformations of the systems as solidification proceeds.
c) To investigate the thermal stability of the alloys of different compositions.
d) To investigate the effect of model size on the atomic ordering, structural transformations, and the thermal stability in the alloys.

CHAPTER 3

METHODOLOGY AND PROCEDURE

3.1 Molecular Dynamics

Molecular Dynamics (MD) is a direct simulation technique at atomic level based on the movement of atoms and molecules. MD predicts the physical properties of the material by solving the Newton's equation of motion over a short pre-defined time interval. By studying the time evolution of an energy-minimized atomic/molecular system MD allows the prediction of thermodynamics and transport properties directly from the underlying interactions between the atoms. Initial position and velocities are assigned to the system then a thermodynamic condition is introduced that causes movement in the atoms and the new forces are calculated. The microscopic information thus obtained is converted to the macroscopic observables by using statistical mechanics. MD simulations generate information at the microscopic level, including the atomic positions and velocities. The conversion of this microscopic information to macroscopic observables such as pressure, energy, heat capacity, and transport properties require statistical mechanics. MD uses classical mechanics to predict the time-dependent trajectories [56] and calculates the "real dynamics", i.e. the behavior of the system, from which the time averages of the system's properties can be calculated. In MD the state of the system at any future time can be predicted from its current state which makes MD a deterministic technique. **Eq. 3-1** is the second Newton's equation of motion where force

(F) is related to the mass (m) and the acceleration (a). Position (R) is a function of time and determines the trajectory of the atoms. The force on each atom is related to the potential energy by **Eq. 3-2**.

$$\vec{F} = m\vec{a} = \frac{d^2\vec{R}}{dt^2}$$ **Eq. 3-1**

$$\vec{F} = -\nabla\vec{E}_{pot}$$ **Eq. 3-2**

3.1.1 Integration Methods

The differential equation (Eq. 3-1) is solved by using integration algorithms. The time integration algorithms are based on finite difference methods [55], where time is discretized with a time step Δt that is the distance between consecutive points on the grid created. The integration scheme gives the positions and some of their time derivates at a certain time t + Δt once those quantities are known on the previous time t. The time evolution of the system can be followed by iterating this procedure. The Verlet algorithm is time reversible, accurate, stable, and minimizes the force calculations [91]. In this work, we have selected the Verlet scheme and will discuss in detail about this in the upcoming section.

3.1.1.1 *Verlet Algorithm*

The Verlet algorithm is one of the most commonly used integration methods in MD simulations. It is a combination of two Taylor expansions for positions r(t), one forward and the other backward in time. If it is written until third-order there are going to appear the velocities, v(t); the accelerations, a(t); and third order derivates of the position b(t). The forward Taylor expansion is explained by **Eq.3-3** and the backward Taylor expansion is explained by **Eq.3-4.**

$$r(t+\Delta t) = r(t) + v(t)\Delta t + \frac{1}{2}\, a(t)\Delta t^2 + \frac{1}{3!}\, b(t)\Delta t^3 + 0(\Delta t^4) \qquad \textbf{Eq. 3-3}$$

$$r(t-\Delta t) = r(t) - v(t)\Delta t + \frac{1}{2}\, a(t)\Delta t^2 - \frac{1}{3!}\, b(t)\Delta t^3 + 0(\Delta t^4) \qquad \textbf{Eq. 3-4}$$

The combination of Eq. 3-3 and Eq. 3-4 gives;

$$r(t+\Delta t) = 2r(t) - r(t-\Delta t) + a(t)\Delta t^2 + 0(\Delta t^4) \qquad \textbf{Eq. 3-5}$$

which is the Verlet's algorithm for positions and is independent of velocities.

3.1.2 Timestep

One of the most important user-defined parameters in MD is the timestep (Δt). The computational time and its cost depend on it. Basically, there are two kinds of errors associated with the integration algorithms, the truncation errors and the round-off errors. The truncation error is related to the accuracy of the finite difference method to describe the true solution. These methods are based on a Taylor expansion truncated at some term. However, the round-off errors are related with the particular implementation of the algorithm, such as the finite number of digits used in computer arithmetic's. It must be said that both errors can be reduced by decreasing the Δt, but for large Δt the truncation errors are the ones that dominate. On the other hand, round-off errors decrease slower than the truncation ones with a decreasing Δt and dominate in the small Δt limit.

For a flexible molecule, the timestep should be no greater than 1/10 the time of the shortest period of motion, in other words, it should have an order of magnitude less than the fastest motion. For rigid molecules (translations and rotation), the timestep of 10 fs is suggested. For flexible molecules (translation, rotation, and torsion) 2fs is suggested and for flexible molecules with more degrees of freedom (translation, rotation, torsion, vibration) 1 fs is normally used [92].

3.1.3 Thermodynamic Ensembles

The algorithms used to integrate the Newton's equation of motion conserves the total energy of the system. In MD, in order to replicate the experimental conditions some theoretical tools must be used. These tools are the statistical ensembles also known as the thermodynamic ensembles in MD. There are few different types of thermodynamics ensembles that MD define.

3.1.3.1 *Microcanonical Ensemble*

In the microcanonical ensemble, the total number of the atoms (N), the total volume (V), and the total energy of the system (E) is preserved throughout the simulation and thus this ensemble is commonly referred to an NVE ensemble. This means that the equation of motion is solved without controlling the pressure or the temperature. The isolated systems at equilibrium are in microcanonical ensemble.

3.1.3.2 *Canonical Ensemble*

Canonical ensemble is also known as NVT. In NVT, the total number of atoms (N), the total volume (V), and the temperature (T) throughout the system remains constant. In order to keep the temperature constant an algorithm is necessary. These algorithms are known as thermostats. The NVT ensemble consists in using the Nose-Hoover thermostat that is a deterministic method used to keep the temperature around the average.

3.1.3.3 *Grand-Canonical Ensemble*

Grand-canonical ensemble us also known as isothermal-isobaric ensemble or NPT ensemble where the total number of the atoms (N), the total pressure (P), and the temperature (T) is kept constant during the simulation. The NPT ensemble is very important in chemistry since chemical reactions are usually conducted under the constant pressure condition.

3.2 Force Fields

To run a MD simulation, the force on each particle which is also defined by the gradient of the potential energy function (Eq. 3-2) is needed to be described. Force Fields are the mathematical functions to mode the potential energy of the system. A single atom will be affected by the potential energy function of every atom in the system. The potential energy function of a system is given by **Eq.3-6.**

$$U(\vec{R}) = \sum U_{bond-strech} + \sum U_{angle-bend} + \sum U_{dihedral} + \sum U_{non-bond} \quad \textbf{Eq. 3-6}$$

U$_{\text{bond}}$ = oscillation about equilibrium bond length

U$_{\text{bond-strech}}$ = oscillation of three atoms about equilibrium bond angle

U$_{\text{dihedral}}$ = torsional rotation of four atoms about a central bond or improper dihedrals

U$_{\text{non-bonded}}$ = non-bonded energy terms

3.2.1 Bonded Interactions

The bonded interactions include three types of interactions; stretching along the bond (bond-length), bending between the bonds (bond-angle), and the rotation around the bonds (torsion). The total bonded energy is explained by **Eq.3-7.**

$$E_{bonded} = E_{bond-strech} + E_{angle-bend} + E_{rotation-along-bond} \qquad \textbf{Eq. 3-7}$$

Bond stretching describes the forces acting between two covalently bonded atoms and both the spring constant and the ideal bond length are dependent on the atoms involved as explained in **Eq.3-8.**

$$E_{bond-strech} = \sum k_b(b - b_0)^2 \qquad \textbf{Eq. 3-8}$$

b = distance between two atoms

b_0 = equilibrium distance between them

k_b = spring constant

Angle bending describes the force originating from the deformation of valence angles (bond angles) between three covalently bonded atoms. The spring constant and the ideal angle are also dependent on the type of atoms. The angle bending term is typically described using a harmonic potential **(Eq.3-9)**.

$$E_{angle-bend} = \sum \theta_b(\theta - \theta_0)^2 \qquad \textbf{Eq. 3-9}$$

θ = angle between three atoms

θ_0 = reference angle

θ_b = force constant

The torsional potentials are described by a dihedral angle and coefficient of symmetry around the middle bond. The dihedral could be proper or improper.

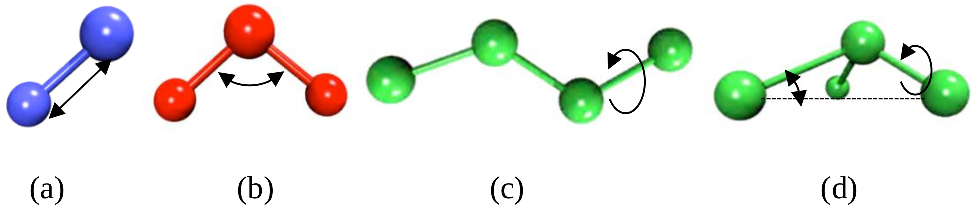

Figure 3-1: The representation of bonded interaction terms contributing to force field: (a) bond stretching, (b) angle bending (c) proper dihedral (c) improper dihedral

3.2.2 Non-Bonded Interactions

There are two types of interactions between non-bonded atoms; Van der Waals potential and Coulombic potential.

$$E_{non-bonded} = E_{van-der-Waals} + E_{electrostatic} \qquad \textbf{Eq. 3-10}$$

These forces act between atoms that are not covalently bonded together. Van der Waals force are relevant when they are close to each other. It is strongly repulsive at short range and weakly attractive at medium range. One of the most widely used functions for van der Waals potential is the Lennard Jones (LJ) potential [93]. LJ potential is given by **Eq.3-11.**

$$V_{LJ} = [4\varepsilon\left(\frac{\sigma}{r}\right)^{12} - \left(\frac{\sigma}{r}\right)^{6}] \qquad \textbf{Eq. 3-11}$$

ε = bonding/dislocation energy

σ = distance where potential energy between two particles is zero

r = distance between two particles

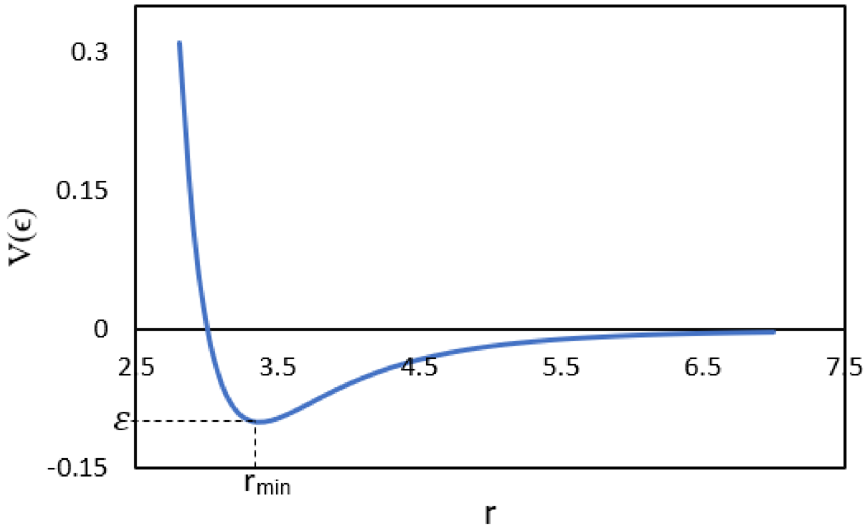

Figure 3-2: The energy vs radius plot in the Lennard-Jones potential interaction

The LJ potential is not used in metal interactions where a delocalized electron sea exists. It fails to accurately predict the metallic material properties. Thus, only a few systems can be modeled using the LJ potential. In the cases of covalent and metallic interactions, a many-body potential is used. For covalently bonded systems, the Stillinger-Weber [94], Reactive potential [95], and Tersoff potential [96] are the mostly used. For metallic systems, the Embedded Atom Method (EAM) [97], Modified Embedded Atom Method (MEAM) [98], Finnis-Sinclair [99] and Glue [100] potentials are typically used.

In electrostatic potential, opposite charges attract and like charges repel. The electrostatic potential energy depends on the amount of charge that each atom contains and the separation distance between the two charges **(Eq.3-12)**.

$$E_{electrostatic} = \sum k \frac{q_1 q_2}{r} \qquad \textbf{Eq. 3-12}$$

q_1 = charge in atom 1

q_2 = charge in atom 2

k = Coulomb's constant

r = distance between charges

3.2.3 Embedded Atom Method

The EAM is a semi-empirical classical many-body potential that is widely used in MD for metallic systems. It provides a computationally efficient description of structural, mechanical, and thermal properties of metallic systems. Daw and Baskes [97] proposed the EAM in 1984. Each atom in EAM is embedded in a host electron gas with a specific density created by all neighboring atoms. The energy required to embed an atom into the density is called an embedding function. For one of the studies, the Zope-Mishin [88] embedded atom method potential created for titanium-aluminum system which was developed by Zope and Mishin in 2003. Zope-Mishin's EAM potential uses ab inito and experimental data for fitting. There are two potential energies that contributes to the total potential energy of the system; the pair-potential energy and the embedding potential energy. The total potential energy in EAM potential is described in **Eq. 3-13.**

$$E_{tot} = \frac{1}{2}\sum_{i,j} \phi_{ij}(r_{ij}) + \sum_{i} F_i\,(\overline{\rho_i}) \qquad \textbf{Eq. 3-13}$$

$(\overline{\rho_i}) = \sum_{j\neq 1} \rho_i\,(r_{ij})$ = the host electron density at site i induced by all other atoms in the system

ρ_i = summation of electron cloud density at the position of atom i

r_{ij} = distance between i atom and j atom

ϕ_{ij} = the pair-potential energy between atoms i and j at positions $\vec{r_i}$ and $\vec{r_j}$

F_i = the embedding potential energy of atom i

For pure systems, the embedding function, pair-wise interaction, and electron gas contribution must be specified. For binary systems, seven functions need to be specified; three pair-wise functions, two embedding functions (one for each type of atom) and two electron gas contribution functions.

3.2.4 Modified Embedded Atom Method

The MEAM is the modified version of EAM and originally was based on the first nearest neighbor interactions, but the improved version of MEAM was developed; which is based on the second nearest neighbor (2NN) interactions instead of the first neighbors. The improved version solves the problems of stability with some bcc elements (Cr, V, Fe) [101]. MEAM was first proposed by Baskes [102] in 1992. MEAM provides a computationally efficient description of structural, mechanical, and thermal properties of metallic systems [103]. In MEAM, an angular dependence of the electron density function is added onto the parameters from EAM. MEAM potentials have been developed for simple cubic [102] and hcp metals [104]. The 2NN-MEAM potentials reproduce the fundamental structural (crystal structure, lattice parameter), thermodynamics, and elastic properties as well as melting point, heat of fusion, bulk solid properties, surface energies, and enthalpy of molten metals. They defined force as follows **(Eq.3-14)**.

$$F_i(\overline{\rho_i}) = AE_c(\bar{\rho}/\overline{\rho^o})\ ln\ (\bar{\rho}/\overline{\rho^o}) \qquad \textbf{Eq. 3-14}$$

A = adjustable parameter

$E_{c\,=}$ sublimation energy

$\overline{\rho^o}$= background electron density for a reference structure

For this study, the 2NN-MEAM potential for titanium-aluminum binary systems developed by Sun-Ramachandranan-Wick [105] at Louisiana Tech University along with the EAM potential developed by Zope-Mishin is used, and a comparative analysis of which potential modeled the titanium-aluminum systems better is done.

3.3 Minimization

Energy minimization is one of the conformational search techniques used prior to conducting a MD simulation. Minimization helps find minimum points in the PES to find the structure with lowest energy. There are different methods of minimization. The first-order minimization methods are steepest descent [106] and conjugate gradient [107]. The second derivative methods are the Newton-Raphson [108] method, Quasi-Newton method, and the Limited-Broyden-Fletcher-Goldfarb-Shanno (L-BFGS) [109] method.

The most commonly used MD minimization methods are typically the steepest descent and conjugate gradient.

3.3.1 Steepest Descent

In the steepest descent method, each search step is performed in the direction of the fastest decrease of the net force. Most implementations have a step size with predetermined default value. If the first step has a decrease in energy, the step size is increased by a factor for the next iteration. If the energy increases, the step size is decreased by a factor. By iterations the minimum is gradually restricted to an even smaller region. The direction of gradient is determined by largest interatomic forces, so it is good for relieving the highest energy features in the initial configuration.

3.3.2 Conjugate Gradient

The steepest descent method may not be efficient because it could get into the zigzag pattern and repeat the same search directions many times. This problem is avoided in the conjugate gradient method, which does not repeat any previous search direction and converge in any number of iterations. The conjugate gradient method generally finds the minimum in fewer steps than the steepest descent method. However, there might be problems when the initial conformation is far from a minimum.

3.4 Computational Procedure and Simulation

The goal of this study is to conduct computer simulations of nanoparticles of different compositions of titanium and aluminum and understand the segregation behavior along with material properties to identify the best composition for powder feed in SLM process. This study is divided into two parts:

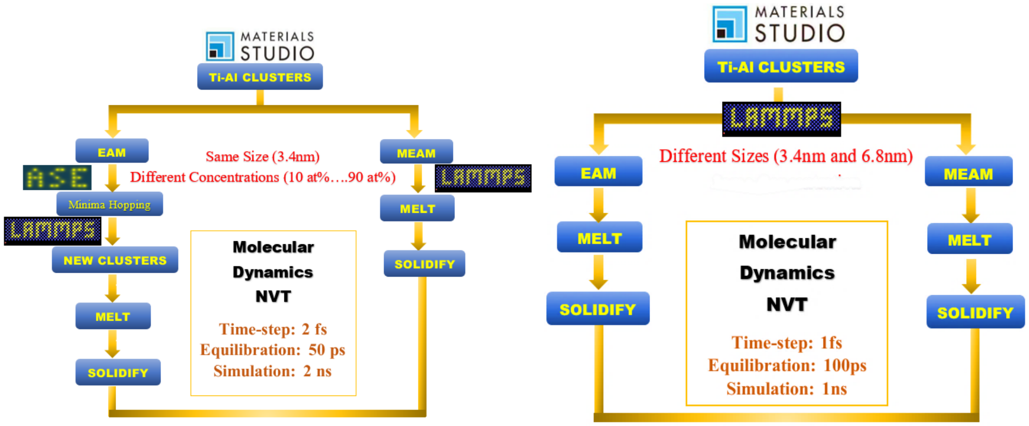

(a) (b)

Figure 3-3: The flowchart summarizing the works done in (a) study1 and (b) study2

In the first study, a comparative study of the structural evolution and solidification of 11 titanium-aluminum nanocluster models with different concentrations, using two different forcefields is done. The size of all the models are the same i.e. the models have 1000 atoms and their diameter is 3.4 nm. The simulation parameters for this study are the time step of 2 fs, equilibration time of 50 ps, and the total simulation time of 2 ns. These parameters give the cooling rate of $2.2x10^{12}$ K/s for this simulation.

In the second study, the comparison of results obtained from two different forcefields but on two models of varying sizes and the same concentration is done. The simulation parameters for this study are the time step of 1 fs, equilibration time of 100 ps, and the total simulation time of 1ns, which gives the cooling rate of $1.1x10^{12}$ K/s for this simulation.

3.4.1 Initial Configuration

Eleven different titanium-aluminum nanoclusters with varying at% are modeled using the Materials Studio 6.0 software [110]. First, the most stable configurations of the clusters are identified using minima hopping and the EAM potential. MEAM potential is not supported by the Atomic Simulation Environment, therefore, for the studies with MEAM potential, the initial cluster models obtained from Materials Studio are the input structures. The simulation is first run using the EAM potential and again using the MEAM potential. The clusters used in this study are pure aluminum, Ti_1Al_9 with 10 at% titanium and 90 at% aluminum, Ti_2Al_8 with 20 at% titanium and 80 at% aluminum, all the way to 100 at% titanium. Table 3-1 shows the number of titanium and aluminum atoms in each modeled cluster.

Table 3-1: Cluster models with respective number of titanium and aluminum atoms

No. of Ti and Al	At% Ti	At% Al	Cluster Names Used
$Ti_{60}Al_{940}$	10	90	Ti_1Al_9
$Ti_{124}Al_{876}$	20	80	Ti_2Al_8
$Ti_{195}Al_{805}$	30	70	Ti_3Al_7
$Ti_{273}Al_{727}$	40	60	Ti_4Al_6
$Ti_{361}Al_{639}$	50	50	Ti_5Al_5
$Ti_{458}Al_{542}$	60	40	Ti_6Al_4
$Ti_{568}Al_{432}$	70	30	Ti_7Al_3
$Ti_{693}Al_{307}$	80	20	Ti_8Al_2
$Ti_{835}Al_{165}$	90	10	Ti_9Al_1

3.4.2 Minima Hopping Method

Minima hopping is a global optimization method first proposed by Stefan Goedecker [111] in 2004. Briefly, this scheme starts with an atomic configuration that has been optimized to any local minimum in the potential energy surface of the metal system under investigation. The metal atoms are then thermalized or given kinetic energy according to a Maxwell–Boltzmann distribution corresponding to a specified initial temperature T_0 and allowed to evolve in a microcanonical (NVE) molecular dynamics simulation with the time per step of 1 fs. A combination of standard steepest descent and conjugate gradient methods is used to perform the geometry relaxations. As the molecular dynamics evolves, the potential energy of the simulation is monitored. After each local optimization, two possibilities exist:

- If any minimum that is on the minima list, including the previous minimum, is re-found, the initial thermalization temperature T_0 is increased by a fixed percent and the simulation is restarted from the previous minimum.
- If a new minimum is found, T_0 is decreased by a fixed percent and the algorithm decides whether to accept or reject the new minimum. This acceptance criterion is parameterized in a simple energy difference, E_{diff}. If the new minimum is not more than E_{diff} higher than the previous minimum, the new configuration is accepted, the configuration is added to the list of previous minima, E_{diff} is decreased by a fixed percent, and the next molecular dynamics step begins from this new minimum. If the new minimum is too high in energy (that is, greater than E_{diff} above the last minimum), the new minimum is rejected, E_{diff} is increased by a fixed percent, and the next molecular dynamics step begins from the previous configuration. Thus, by continuously adjusting the parameters T_0 and E_{diff}, the

algorithm can effectively sample the relevant regions of the potential energy surface of a given system.

The first part of this study utilizes the minima hopping method to identify the global minimum structure within the user specified number of steps, which is the input structure for the solidification simulation. The simulation is run in the Atomic Simulation Environment (ASE) [112] on Louisiana Tech's Cerberus cluster. In this simulation only 20 hop steps are initiated so the local minimum is not necessarily the global minimum of the cluster. A Portable Batch System (PBS) script is written to perform parallel computing. 4 nodes and 2 processors with the maximum wall time of 144 hours are selected. The computations are completed in about 4 hours for all the clusters in parallel computing, whereas it took about 13 hours per cluster on a single processor. The initial configuration of Ti_1Al_9 obtained from Materials Studio software and the configuration obtained after minima hopping is shown in **Figure 3-4.**

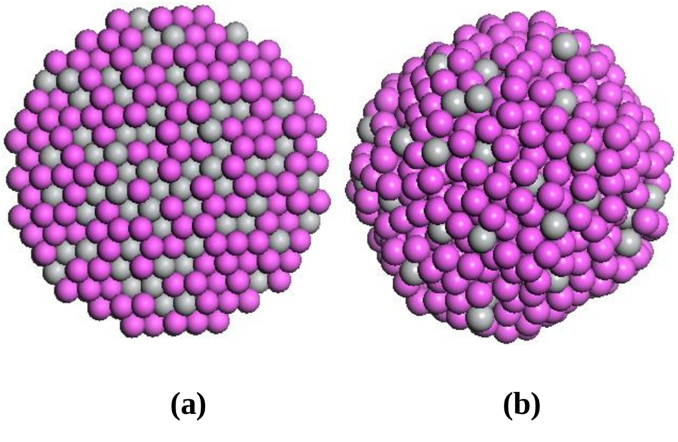

(a) (b)

Figure 3-4: (a) The random initial configuration of Ti_1Al_9 from Materials Studio (b) the energy minimized Ti_1Al_9 obtained from minima hopping (Grey: Ti, Pink: Al)

3.4.3 Solidification

After identifying the minimum configurations for the EAM models using minima hopping, the solidification study is conducted. The clusters are first melted at either 2000K or 2500K depending on the composition of the alloys, then solidified at room temperature (300K). Large-scale Atomic/Molecular Massively Parallel Simulator (LAMMPS) [113] is chosen to perform simulations for this study. LAMMPS is a free software provided by Sandia National Laboratories. LAMMPS can model metallic, atomic, and biological systems using different forcefields. LAMMPS can also simulate large systems with millions of particles with accuracy.

To run a MD simulation in LAMMPS, an input script is written along with a potential library file. The input script is the set of executable commands and the potential file contains all the parameters for the interatomic interactions. The system type is defined to be 3D with the periodic boundary condition. The atomic masses for each element type are defined along with the simulation box size (60 Å). The atom masses of titanium (47.867 amu) and aluminum (26.982 amu) [114] and the simulation box size are predefined when the Material's Studio coordinate file was converted to the LAMMPS readable .data file using a self-written python script.

The clusters are first minimized with the energy convergence criteria of 10^{-6} and the force tolerance of 10^{-6} force units. Then the simulation is initiated with a random velocity using the NVT ensemble. Initially all models are melted at 2500 K in LAMMPS. However, 2500 K was found to be too high for the aluminum rich clusters where they started to vaporize instead of melting. Therefore, pure aluminum, and aluminum-rich (Ti_1Al_9, Ti_2Al_8, Ti_3Al_7, and Ti_4Al_6) clusters are melted at 2000K and pure titanium and titanium-rich (Ti_5Al_5, Ti_6Al_4, Ti_7Al_3, Ti_8Al_2, and Ti_9Al_1) clusters are melted at 2500K. **Figure 3-5 (a)** shows that the atoms in Ti_1Al_9 are scattered far when they are melted at 2500K. This means that the melting temperature of 2500K was too high for aluminum-rich clusters. **Figure 3-5 (b)** shows the same cluster melted at 2000K which shows a better melted cluster. The same is observed when the MEAM potential is used.

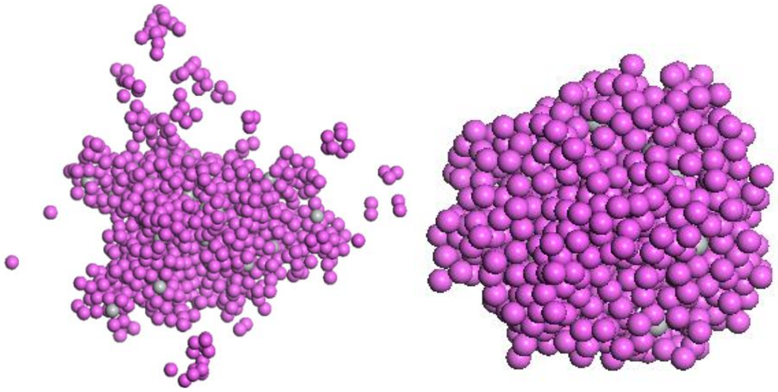

(a) (b)

Figure 3-5: The comparison of (a) Ti_1Al_9 at 2500K vs (b) Ti_1Al_9 at 2000K using the EAM potential

The structures are equilibrated for 50 ps to obtain the equilibrium melted structures. For the melting, the timestep of 2 fs is chosen. The potential energy, kinetic energy, and the total energy of atoms were recorded. Then the melted clusters are solidified using the NVT ensemble and Nose-Hoover thermostat by reducing the temperature to 300K. The models are assigned an initial velocity then solidified with the timestep of 2 fs, iteration steps of 1,000,0000, and the total simulation time of 2 ns. The potential energies at different temperatures are recorded for post processing to evaluate the properties and changes in the atomic structures.

CHAPTER 4

RESULTS AND DISCUSSION: EMBEDDED ATOM METHOD

The results on structural transformations and the segregation obtained using the Zope-Mishin's EAM potential are discussed in this chapter.

4.1 Structural Evolution of the Clusters

In this section the structural transformations of each cluster models at different temperatures when they are solidified after melting in high temperature are discussed. **Figure 4-1** shows the evolution of Ti_1Al_9 clusters at different temperatures when the EAM potential is used.

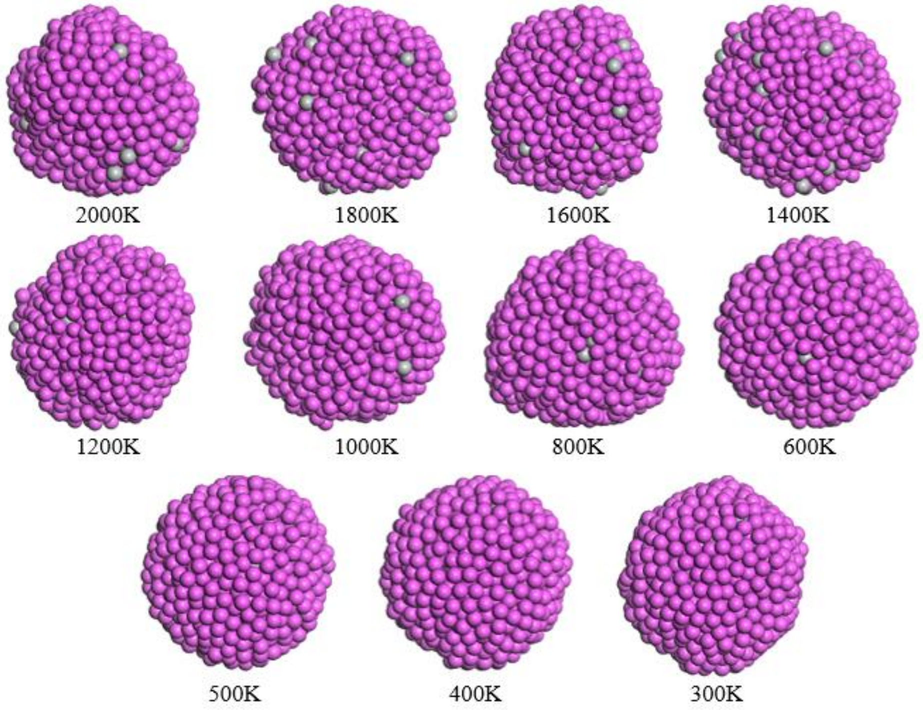

Figure 4-1: The Ti_1Al_9 clusters at different temperatures as it solidifies using the EAM potential.

At 2000K, the cluster seems to be well-mixed and in liquid state. Few titanium atoms (gray) can be seen on the surface. Upon solidification, a distinct geometric change in the cluster is visible. The initial spherical cluster geometry changed to a structure with visible vertices, however, not distinct. The titanium atoms seem to have moved to the inner core of the cluster with an abundance of the aluminum atoms (pink) on the surface. Similarly, on all the other cases, at melting, the atoms seem disoriented and at 300K the atoms seem to have compacted themselves together to form distinct geometries **(Figure 4-2).**

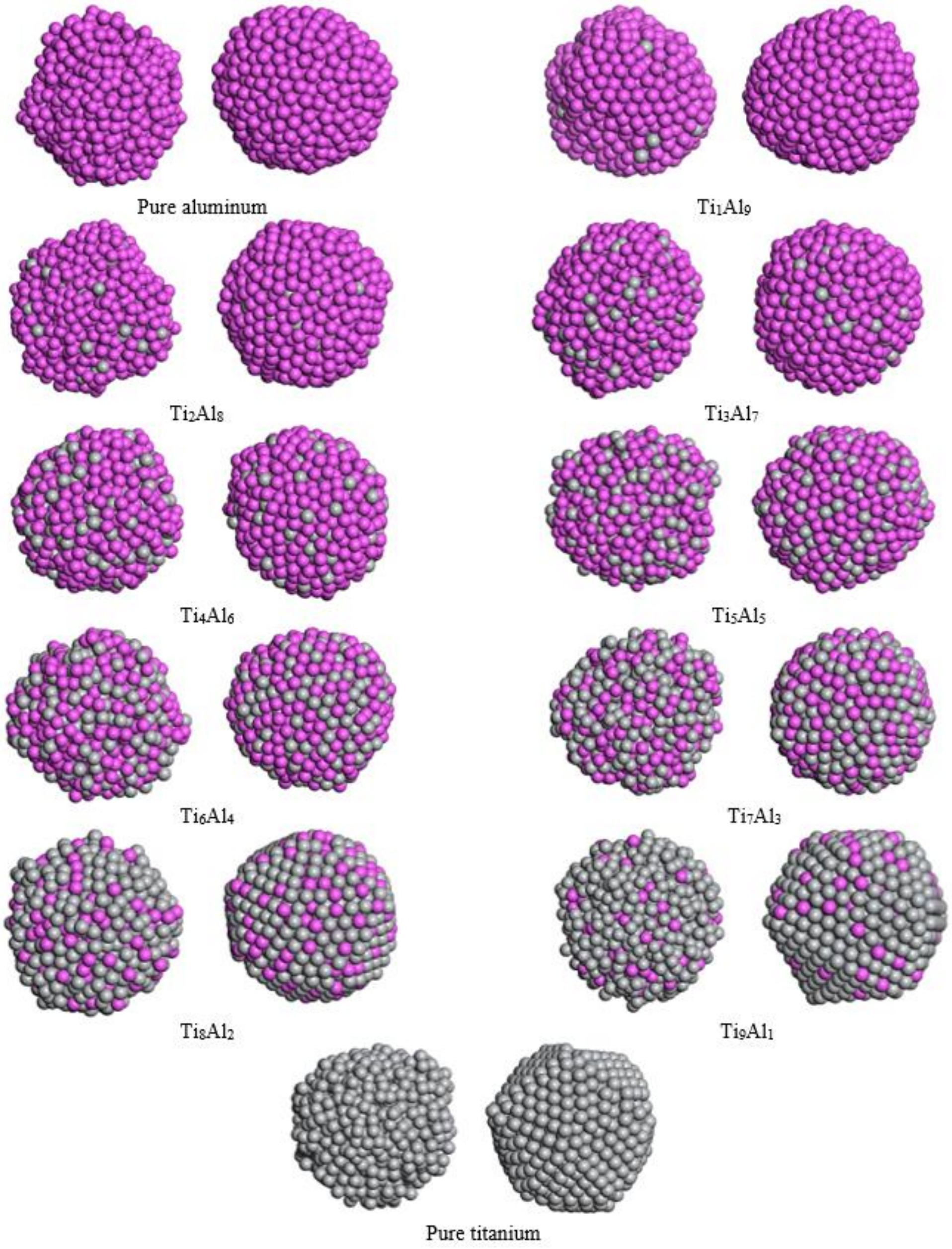

Pure aluminum

Ti_1Al_9

Ti_2Al_8

Ti_3Al_7

Ti_4Al_6

Ti_5Al_5

Ti_6Al_4

Ti_7Al_3

Ti_8Al_2

Ti_9Al_1

Pure titanium

Figure 4-2: The melted (left) and solidified (right) surface structures of all cluster models obtained using the EAM potential. The model names are labeled.

From Figure 4-2, at 300K, the clusters with higher titanium concentration (Ti_8Al_2, Ti_9Al_1, and pure titanium) seem to have more ordered arrangement than the clusters with high aluminum concentration. Visually, these titanium-rich clusters seem to have facets that resemble an icosahedron **(Figure 4-3)**.

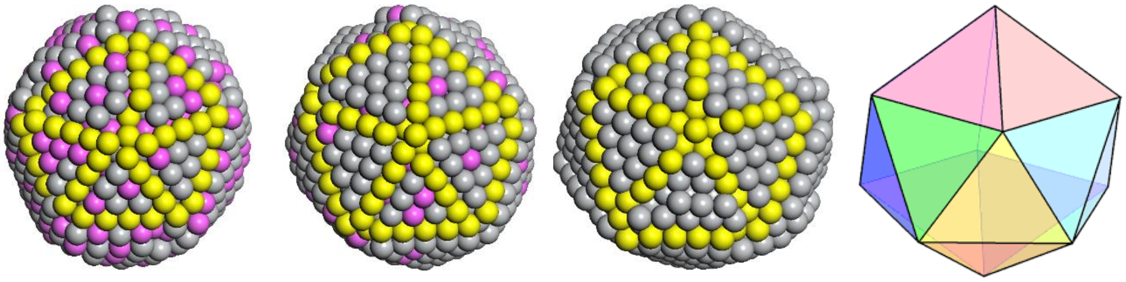

Ti_8Al_2 Ti_9Al_1 Pure titanium Typical icosahedron

Figure 4-3: The Ti_8Al_2, Ti_9Al_1, and pure titanium at 300K obtained from the EAM potential vs a typical icosahedron, yellow highlighted atoms for easy visualization of the facets.

Usually, the structures of nanoclusters are different from the structure of nanocrystals which resemble the structure of bulk crystals. Icosahedron is a polyhedron with 20 faces. The faces are triangular, and the combination of triangular faces forms a pentagon. In Figure 4-3, the triangular faces (highlighted with yellow) tries to form an imperfect pentagon. Sharp visible facets are observable in these clusters at it is in a typical icosahedron. The importance of such geometry formation is associated with the stability, however, computational methods such as Density Functional Theory (DFT) [115] should be used to further study the stability of the clusters.

Additionally, the cooling rate influences the microstructure greatly. During rapid solidification (SLM) of metals, amorphous or crystalline are formed depending on the cooling rate. Faster cooling rate causes little time for crystal nucleation so amorphous structures can be observed whereas the slower cooling rate provides longer incubation time for atoms and have more chances to occupy the low energy position forming crystals. While the critical cooling rate for amorphization of conventional alloys is in the order of 10^6 K/s, the critical rate for pure metals is beyond 10^{12} K/s. In this study, the cooling rate of $1.1\text{x}10^{12}$ K/s is used. At such high cooling rate, nucleation of the clusters is evident.

4.2 Atom Segregation

In this section, metal segregation is studied by tracking the concentration of each type of atoms at different radial distances from the core at different temperatures. The density of atoms is the number of atom type “i” at each radial distance in 2Å intervals divided by the total number of atoms type “i” in the whole cluster. The atomic density is given by **Eq.4-1** and the schematic representation of the radial density distribution of atoms is shown in **Figure 4-4.**

$$\rho_i = \frac{n_i}{n} \qquad \textbf{Eq. 4-1}$$

ρ_i=atomic density

n_i=number of atom type i at given radial distance

n=total number of atom type i in the cluster

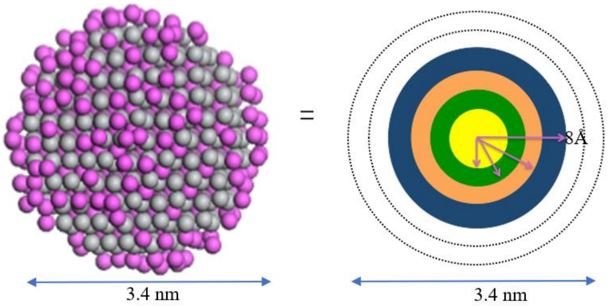

Figure 4-4: The schematic representation of the radial density distribution of atoms from the core of the cluster.

Figure 4-5 – Figure 4-13 represents the plots of radial distances (Å) against the atomic density (ρ_r) for all clusters. The gray line represents the concentration profile of titanium and the pink line represents that of aluminum.

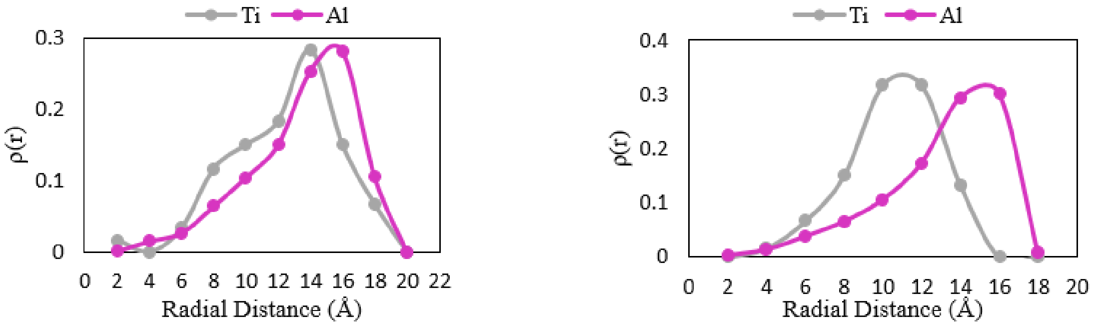

Figure 4-5: The atomic radial density distribution of titanium (Ti) and aluminum (Al) in Ti_1Al_9 cluster at melted (left) and solidified (right) state obtained using the EAM potential.

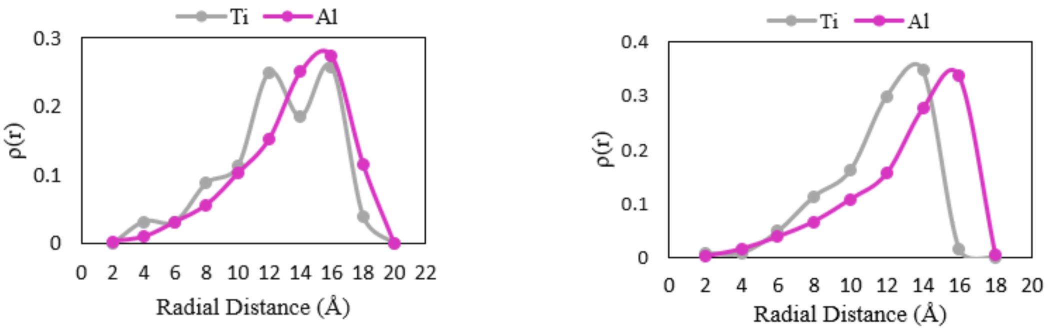

Figure 4-6: The atomic radial density distribution of titanium (Ti) and aluminum (Al) in Ti_2Al_8 cluster at melted (left) and solidified (right) state obtained using the EAM potential.

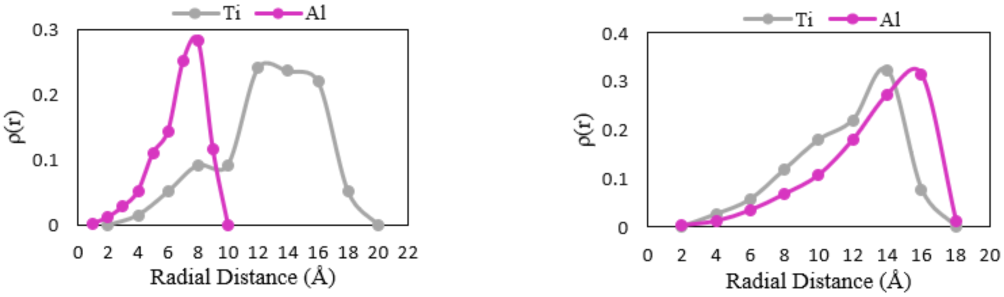

Figure 4-7: The atomic radial density distribution of titanium (Ti) and aluminum (Al) in Ti_3Al_7 cluster at melted (left) and solidified (right) state obtained using the EAM potential.

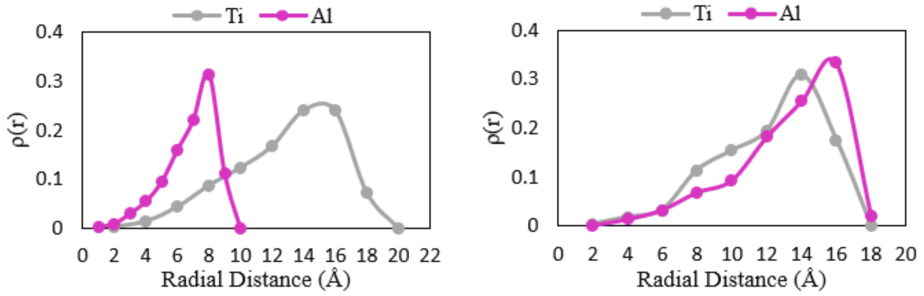

Figure 4-8: The atomic radial density distribution of titanium (Ti) and aluminum (Al) in Ti_4Al_6 cluster at melted (left) and solidified (right) state obtained using the EAM potential.

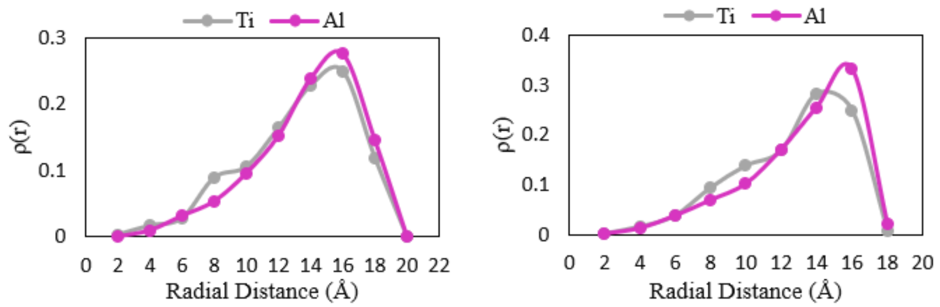

Figure 4-9: The atomic radial density distribution of titanium (Ti) and aluminum (Al) in Ti_5Al_5 cluster at melted (left) and solidified (right) state obtained using the EAM potential.

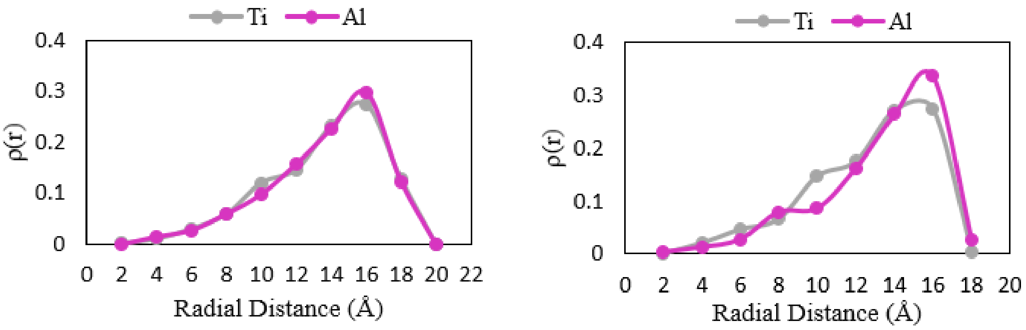

Figure 4-10: The atomic radial density distribution of titanium (Ti) and aluminum (Al) in Ti_6Al_4 cluster at melted (left) and solidified (right) state obtained using the EAM potential.

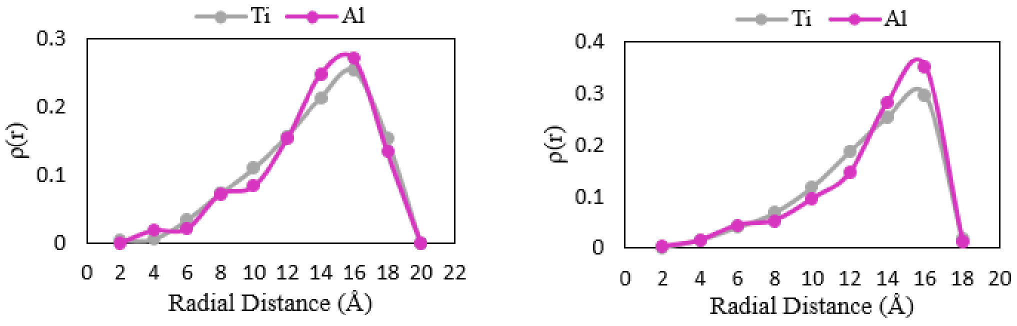

Figure 4-11: The atomic radial density distribution of titanium (Ti) and aluminum (Al) in Ti_7Al_3 cluster at melted (left) and solidified (right) state obtained using the EAM potential.

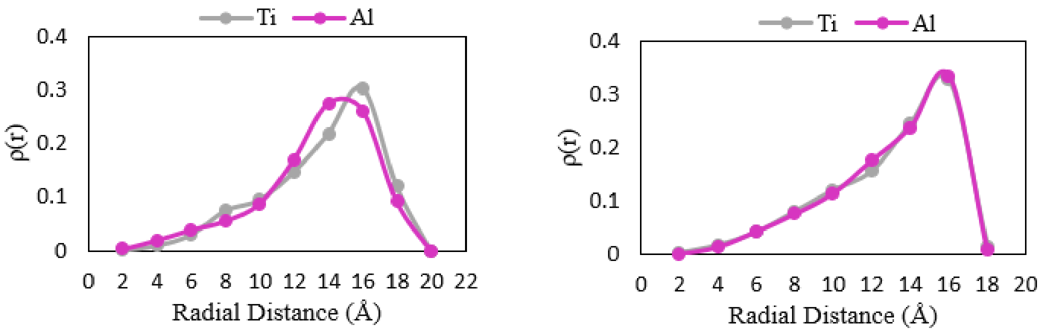

Figure 4-12: The atomic radial density distribution of titanium (Ti) and aluminum (Al) in Ti_8Al_2 cluster at melted (left) and solidified (right) state obtained using the EAM potential.

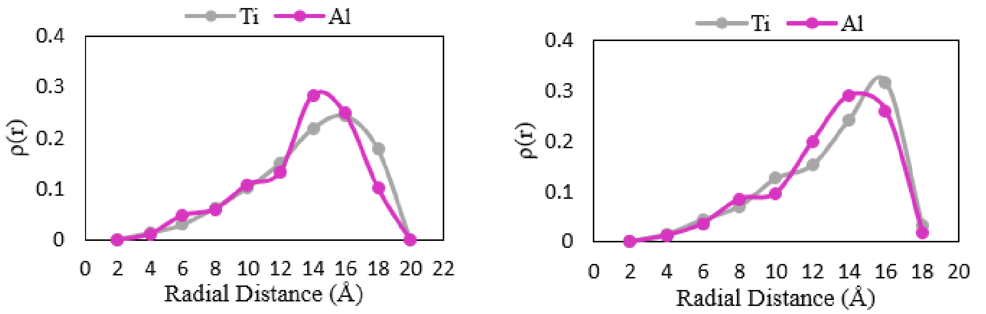

Figure 4-13: The atomic radial density distribution of titanium (Ti) and aluminum (Al) in Ti_9Al_1 cluster at melted (left) and solidified (right) state obtained using the EAM potential.

In all the models, titanium atoms seem to have concentrated around the radial distance of 14-16 Å in the liquid state. Upon solidification, titanium shifts a little towards the core of the cluster at the radial distance of approximately 12-14 Å. Further, the aluminum atoms in all models except Ti_3Al_7 and Ti_4Al_6 seem to be concentrating at the surface in the liquid state. In Ti_3Al_7 and Ti_4Al_6, aluminum stays at the core of the cluster at the radial distance of approximately 6-8 Å. However, at 300K the aluminum atoms have migrated at the surface at the radial distance of approximately 16-18 Å.

Additionally, a bar chart is created to understand the concentration profile at both temperatures better **(Figure 4-14, Figure 4-15, Figure 4-16, and Figure 4-17).**

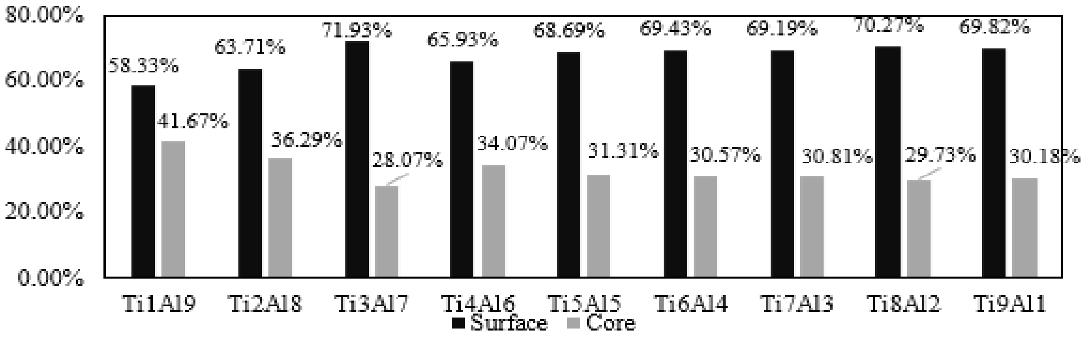

Figure 4-14: The concentration of titanium atoms at 2000K/2500K at the surface and the core of the cluster obtained using the EAM potential.

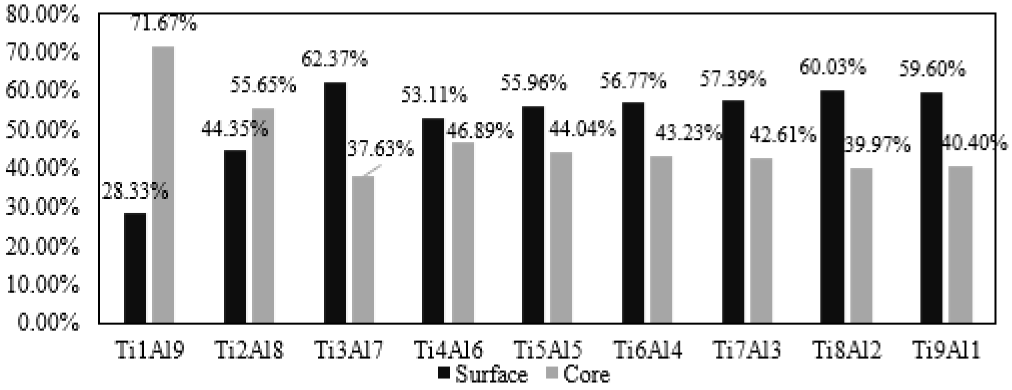

Figure 4-15: The concentration of titanium atoms at 300K at the surface and the core of the cluster obtained using the EAM potential**.**

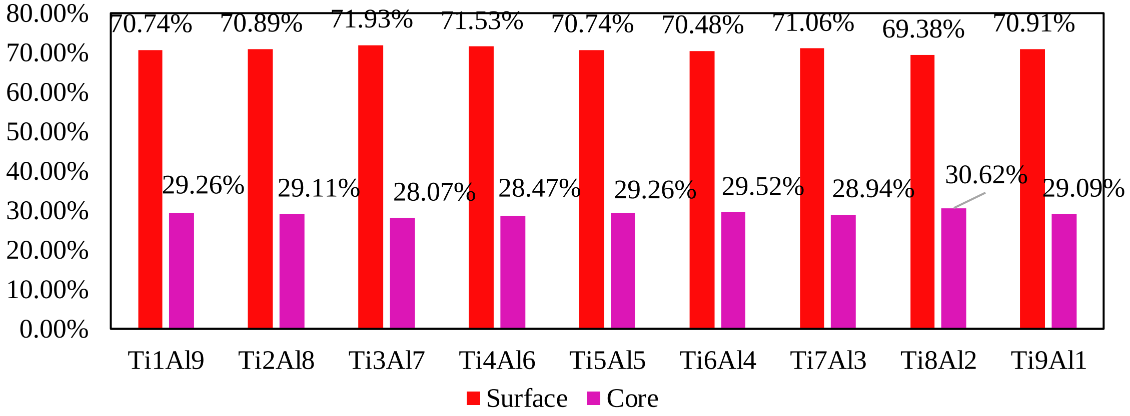

Figure 4-16: The concentration of aluminum atoms at 2000K at the surface and the core of the cluster obtained using EAM potential.

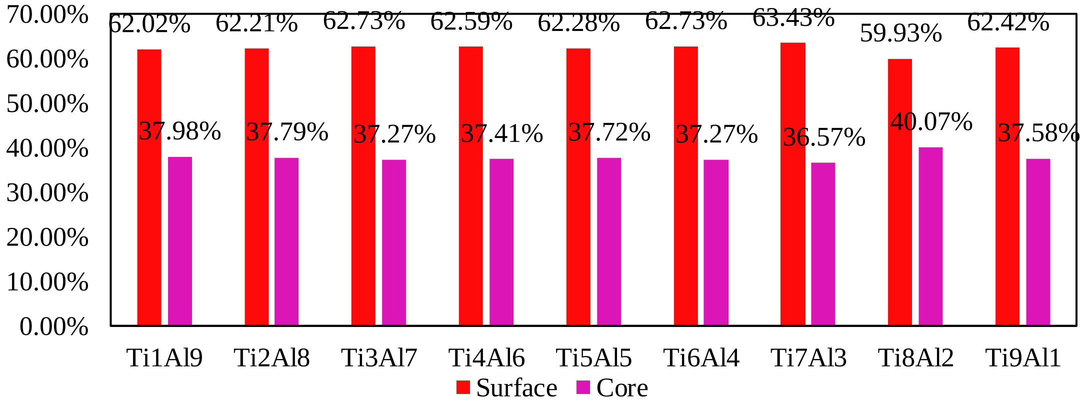

Figure 4-17: The concentration of aluminum atoms at 300K at the surface and the core of the cluster obtained using the EAM potential.

Figure 4-14 and Figure 4-15 represent the concentration profiles of titanium atoms at liquid and solid states. The higher concentration of titanium at the surface in liquid state is clearly visible (Figure 4-14). However, at 300K the concentration seems to have reduced at the surface. This could be because at the solid state the cluster is trying to form a geometry and only a certain number of atoms are accommodated on the surface for the geometry the cluster is trying to form. This also suggests that the geometry of the clusters is changing at different temperatures.

Similarly, Figure 4-16 and Figure 4-17 represent the concentration profiles of aluminum atoms at liquid and solid states. The concentrations at the liquid state seem almost the same (~70%) for all the clusters and upon solidification the concentration trend looks the same with the decrease in concentration at the surface and a slight increase in the concentration at the core.

CHAPTER 5

RESULTS AND DISCUSSION: MODIFIED EMBEDDED ATOM METHOD

The results on the structural transformations and the segregation obtained using the Sun-Ramachandranan-Wick MEAM potential are discussed in this chapter.

5.1 Structural Evolution of the Clusters

In this section, the structural transformations of each cluster models at different temperatures when they are solidified after melting in high temperature using the MEAM potential are discussed. **Figure 5-1** shows the evolution of Ti_1Al_9 clusters as the temperature changes.

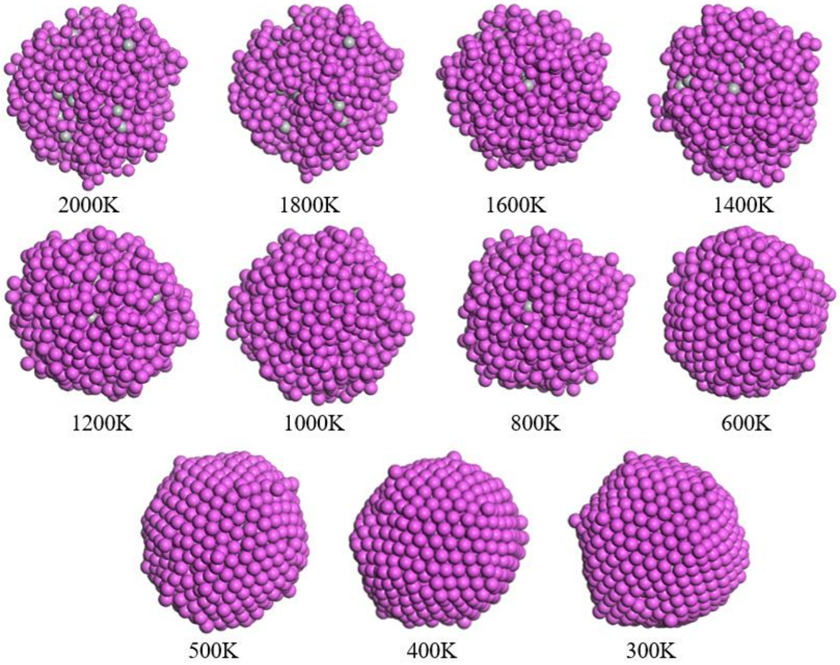

Figure 5-1: The Ti_1Al_9 cluster at different temperatures as it solidifies using the MEAM potential.

At 2000K, the cluster seems to be well-mixed and in liquid state and at 300K the clusters have solidified and starts to form some kind of geometry. Unlike the EAM potential the clusters at 300K show that the outer layer is completely covered by aluminum.

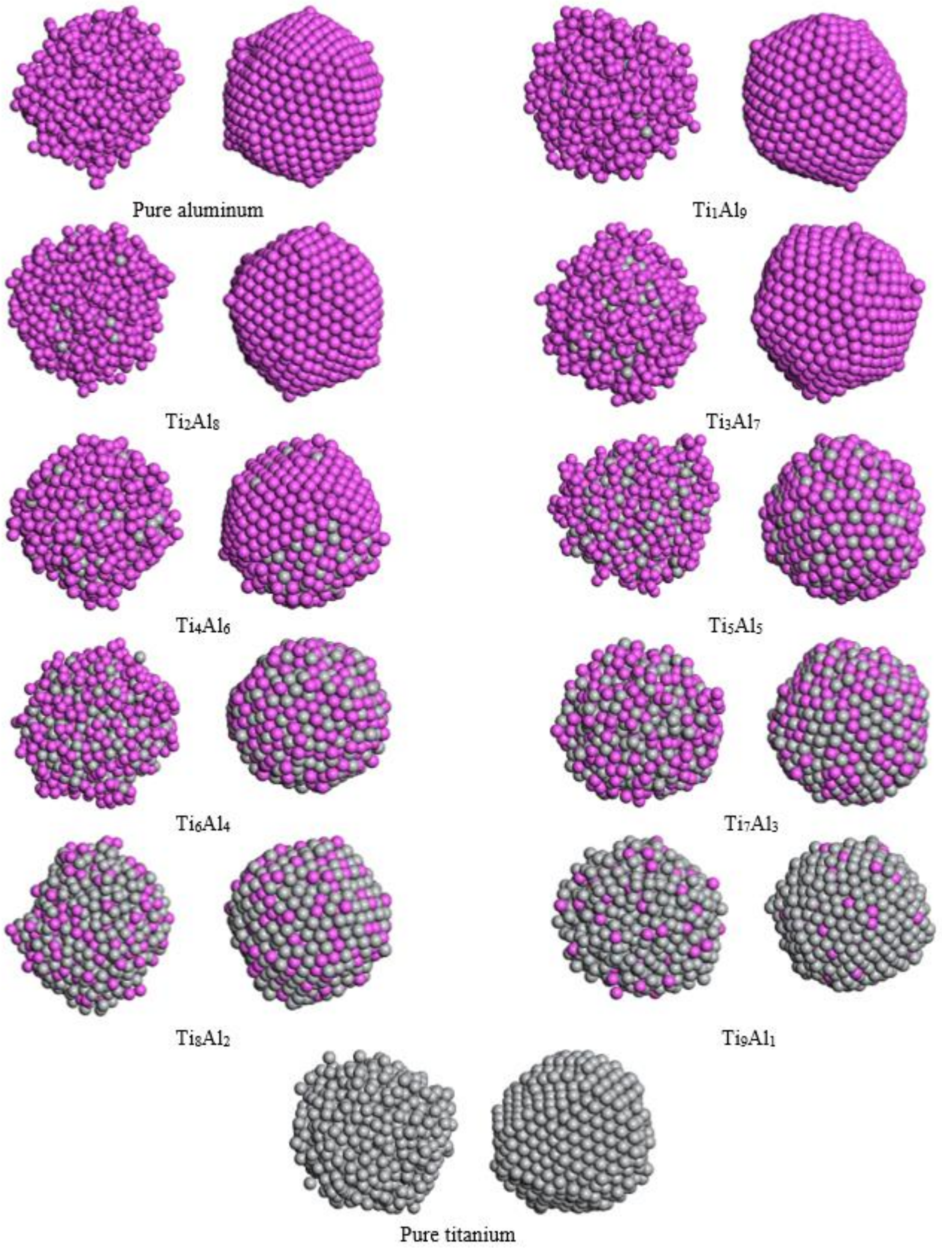

Pure aluminum

Ti_1Al_9

Ti_2Al_8

Ti_3Al_7

Ti_4Al_6

Ti_5Al_5

Ti_6Al_4

Ti_7Al_3

Ti_8Al_2

Ti_9Al_1

Pure titanium

Figure 5-2: The melted (left) and solidified (right) surface structures of all clusters modeled obtained using the MEAM potential. The model names are labeled.

From Figure 5-2, the clusters with higher aluminum concentration (Pure aluminum, Ti_1Al_9, and Ti_2Al_8) seem to have more ordered arrangement than the clusters with high titanium concentration at 300K. Visually, these aluminum-rich clusters seem to have facets that resemble a truncated octahedron **(Figure 5-3)**.

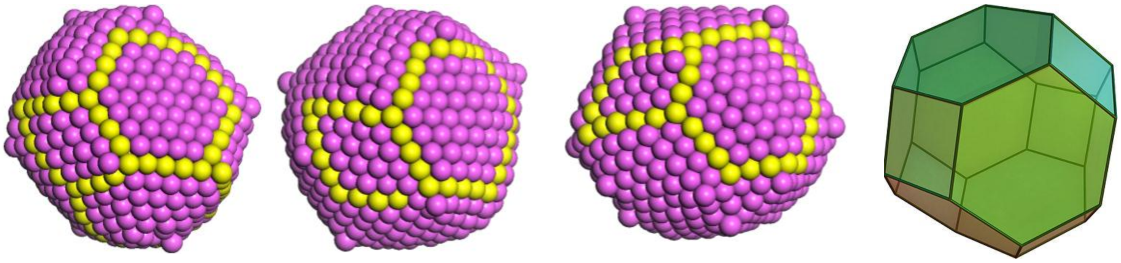

Pure aluminum Ti_1Al_9 Ti_2Al_8 Typical truncated octahedron

Figure 5-3: Pure aluminum, Ti_1Al_9, and Ti_2Al_8 at 300K obtained from the MEAM potential vs the typical truncated octahedron, yellow highlighted atoms are for easy visualization of facets.

A truncated octahedron has fourteen faces with eight hexagonal and six square faces. Tang *et al*. [116] observed that the aluminum clusters with the order of 10^3 (atom number) and higher adopts the truncated octahedron shape upon solidification, which is what is observed in Figure 5-3. Pure aluminum and the aluminum-rich clusters show an inclination to truncated octahedral geometry upon solidification. The hexagonal faces (highlighted in yellow) can be seen in these clusters. However, the titanium-rich clusters do not show any distinct geometry upon solidification in this study.

5.2 Atom Segregation

The atom segregation study for MEAM is carried out the exact way it is done for EAM. (Refer to Eq. 4-1 and Figure 4-4). **Figure 5-4 – Figure 5-12** represents the plot of radial distance (Å) versus the atomic density in all clusters obtained using the MEAM potential.

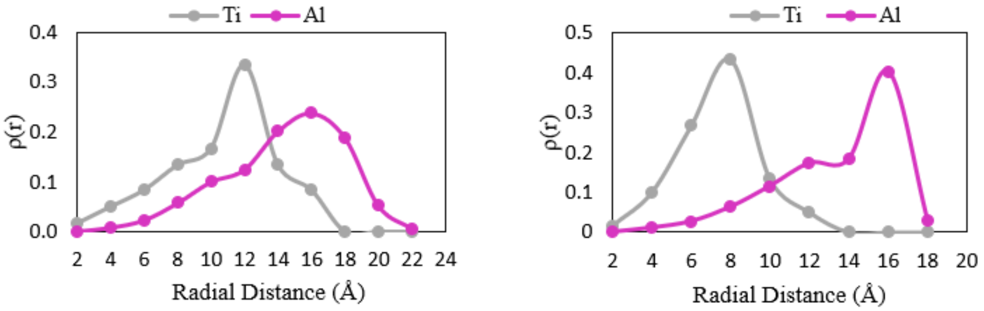

Figure 5-4: The atomic radial density distribution of titanium (Ti) and aluminum (Al) in Ti_1Al_9 cluster at melted (left) and solidified (right) states obtained using the MEAM potential.

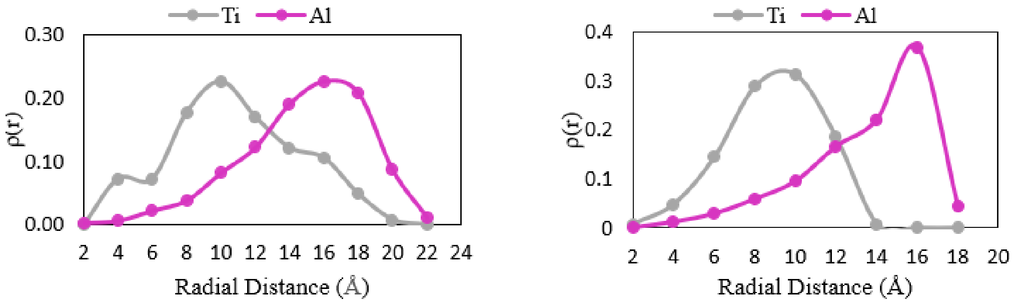

Figure 5-5: The atomic radial density distribution of titanium (Ti) and aluminum (Al) in Ti_2Al_8 clusters at melted (left) and solidified (right) states obtained using the MEAM potential.

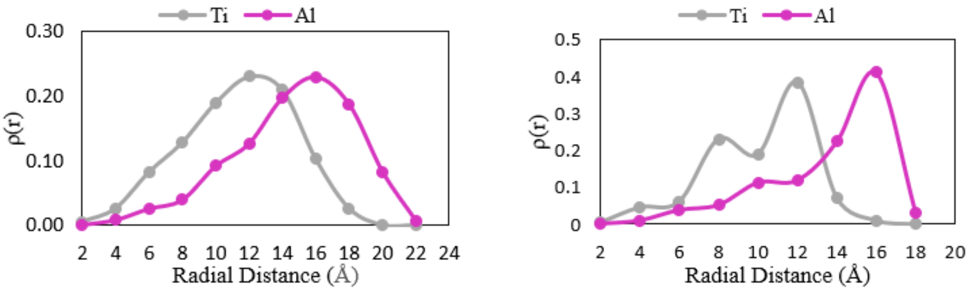

Figure 5-6: The atomic radial density distribution of titanium (Ti) and aluminum (Al) in Ti_3Al_7 clusters at melted (left) and solidified (right) states obtained using the MEAM potential.

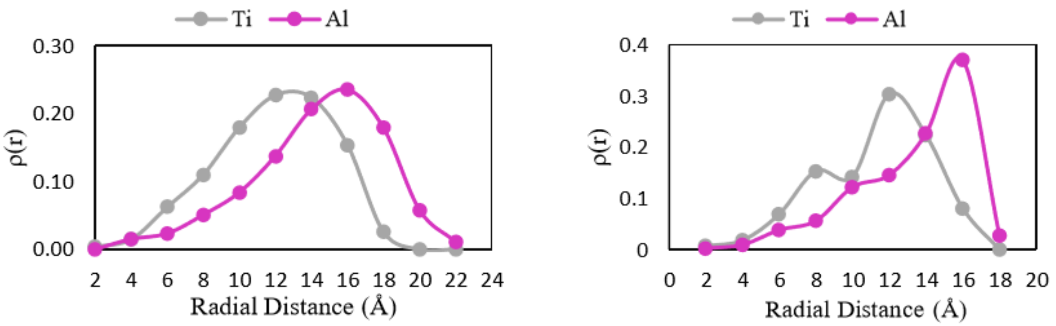

Figure 5-7: The atomic radial density distribution of titanium (Ti) and aluminum (Al) in Ti_4Al_6 clusters at melted (left) and solidified (right) states obtained using the MEAM potential.

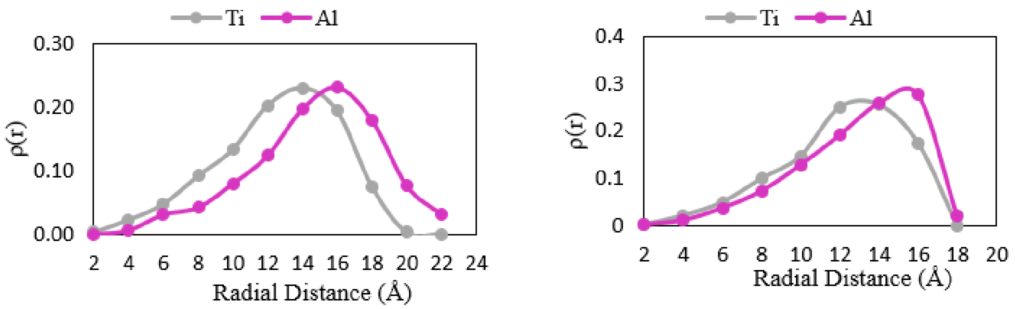

Figure 5-8: The atomic radial density distribution of titanium (Ti) and aluminum (Al) in Ti_5Al_5 clusters at melted (left) and solidified (right) states obtained using the MEAM potential.

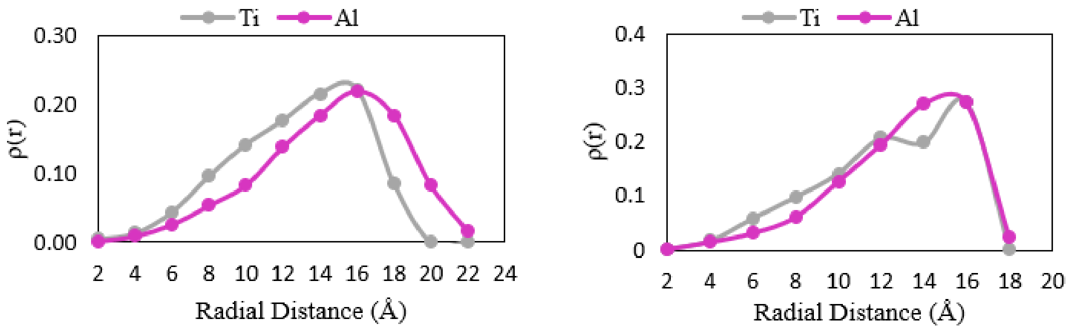

Figure 5-9: The atomic radial density distribution of titanium (Ti) and aluminum (Al) in Ti_6Al_4 clusters at melted (left) and solidified (right) states obtained using the MEAM potential.

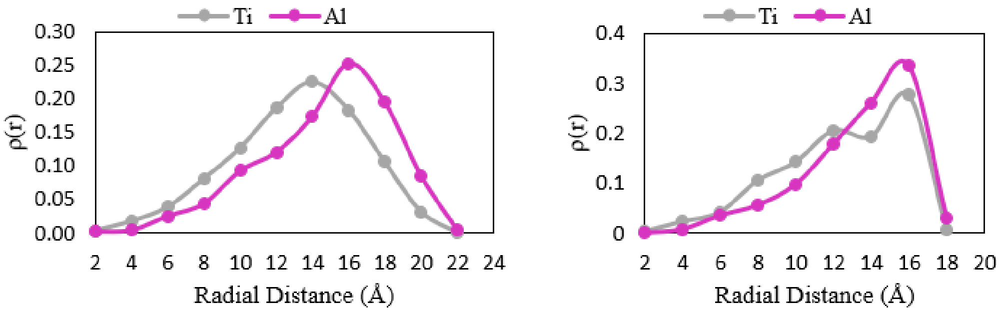

Figure 5-10: The atomic radial density distribution of titanium (Ti) and aluminum (Al) in Ti_7Al_3 clusters at melted (left) and solidified (right) states obtained using the MEAM potential.

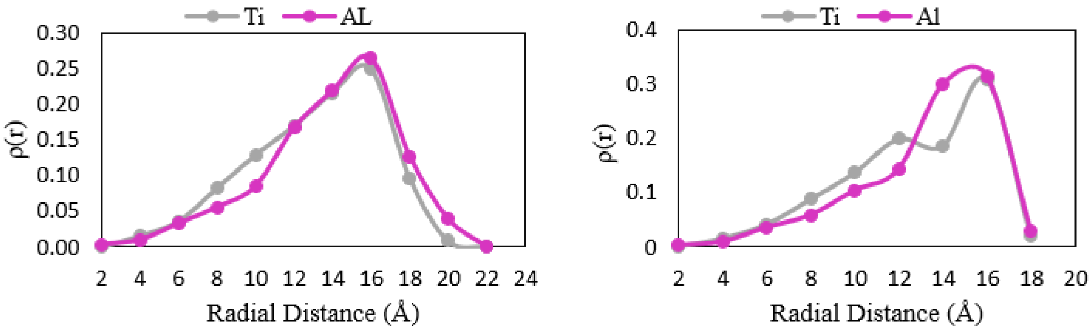

Figure 5-11: The atomic radial density distribution of titanium (Ti) and aluminum (Al) in Ti_8Al_2 clusters at melted (left) and solidified (right) states obtained using the MEAM potential.

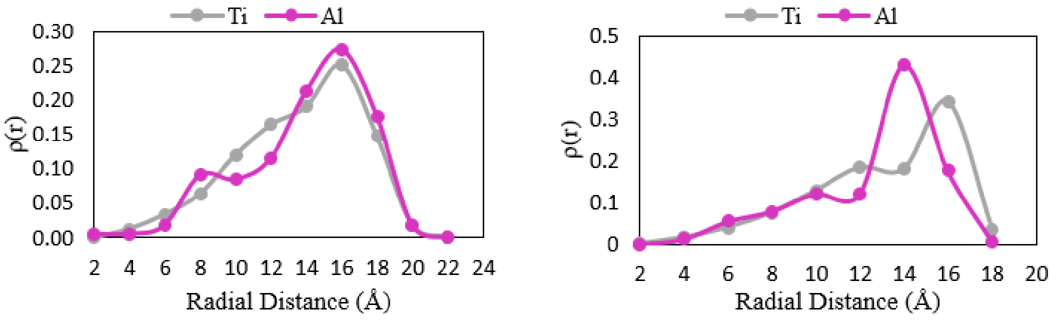

Figure 5-12: The atomic radial density distribution of titanium (Ti) and aluminum (Al) in Ti_9Al_1 cluster at melted (left) and solidified (right) states obtained using the MEAM potential.

The plots suggest that titanium concentrates at core in both liquid and solid states whereas aluminum atoms stay at the surface. In the clusters with 70, 80 and 90 at% titanium, namely, Ti_7Al_3, Ti_8Al_2, and Ti_9Al_1, aluminum is concentrated at the core in the liquid state, whereas, aluminum shifts little bit but not all the way to the surface upon solidification. The titanium-rich MEAM models (Ti_7Al_3, Ti_8Al_2, ad Ti_9Al_1) show low segregation of aluminum and therefore should be further explored for SLM powder creation for better adhesion between the interfacial layers. Aluminum is not preferred on the surface upon solidification because if that is the case, considering the weak aluminum-aluminum bond strength, the adhesion between the two interfacial layers becomes very weak, reducing the overall strength of the 3D printed part.

The following bar charts are created to understand the concentration profile at melting and solidification better **(Figure 5-13, Figure 5-14, Figure 5-15, and Figure 5-16).**

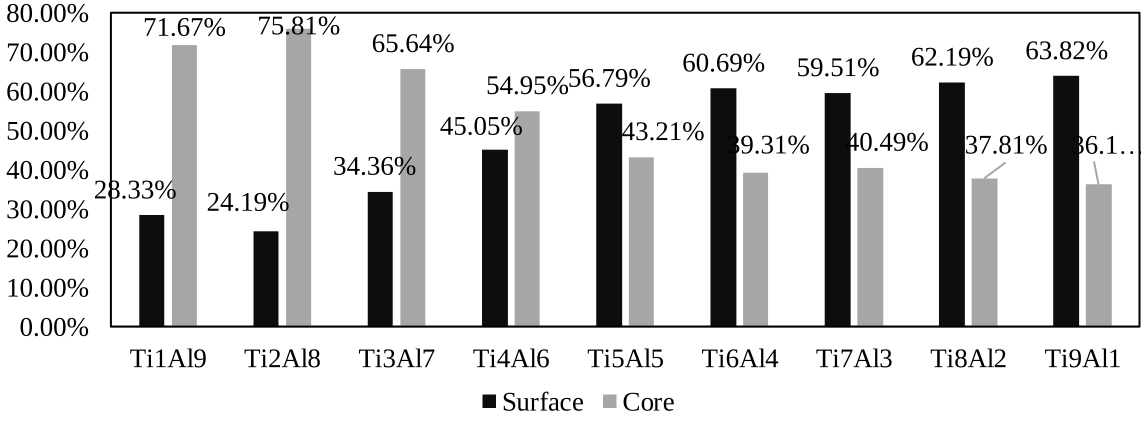

Figure 5-13: The concentration of titanium atoms at 2000K/2500K at the surface and the core of the cluster obtained using the MEAM potential.

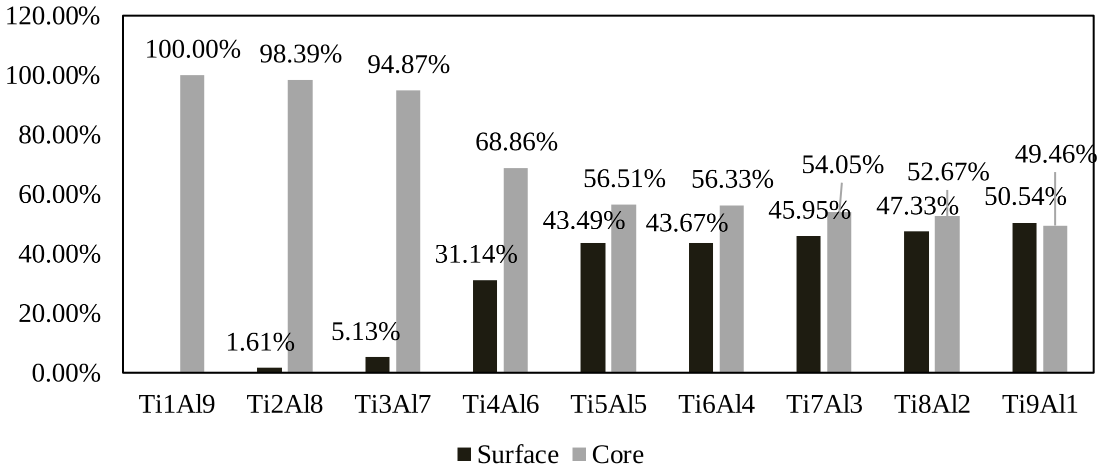

Figure 5-14: The concentration of titanium atoms at 2000K/2500K at the surface and the core of the cluster obtained using the MEAM potential.

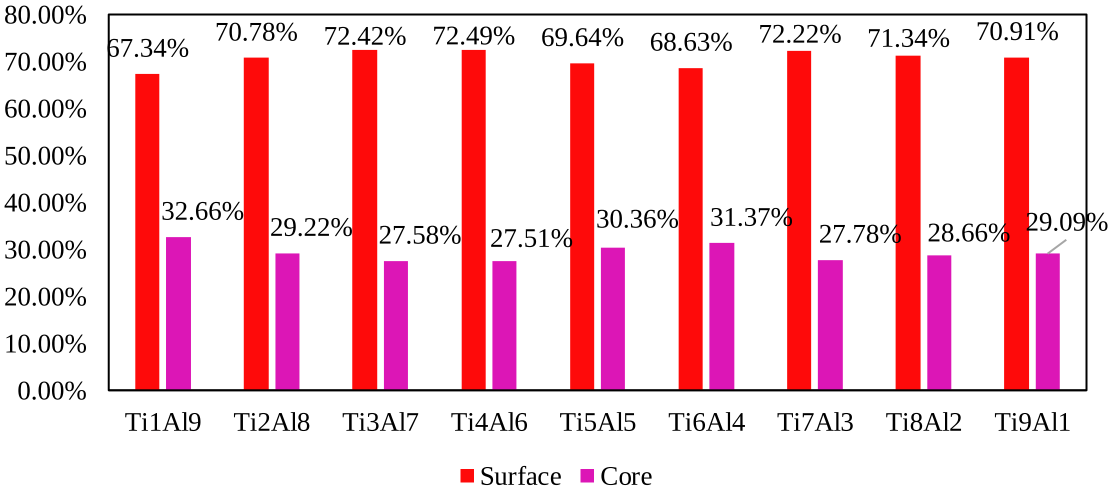

Figure 5-15: The concentration of aluminum atoms at 2000K/2500K at the surface and the core of the cluster obtained using the MEAM potential.

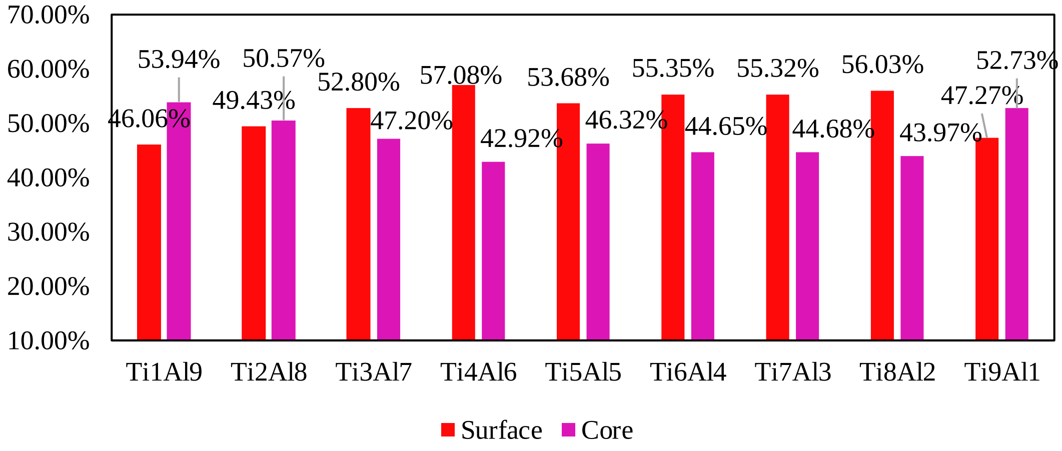

Figure 5-16: The concentration of aluminum atoms at 300K at the surface and the core of the cluster obtained using the MEAM potential.

Figure 5-13 and Figure 5-14 represent the concentration profiles of titanium atoms at liquid and solid states. The concentration of titanium in the aluminum rich clusters (Ti_1Al_9, Ti_2Al_8, Ti_3Al_7, and Ti_4Al_6) on the surface decreases upon solidification. Like in the EAM case, this change in concentration could be because surface geometry of the cluster is changing at low temperature.

Similarly, Figure 5-15 and Figure 5-16 represent the concentration profiles of aluminum atoms at liquid and solid states. The plots show that in all cases aluminum concentrates the most at the surface in the liquid state. However, upon solidification aluminum still stays at the surface but the concentration is significantly reduced. Therefore, aluminum has high surface segregation at liquid state.

5.3 Potential Energy and Heat Capacity Curves

The potential energy and heat capacity curves are created in order to identify the phase change temperatures (melting temperatures) of the clusters obtained using the

MEAM model. This analysis is not done on the EAM clusters. **Figures 5-17 – Figure 5-27** represent the plots of potential energies at different temperatures and the corresponding heat capacity peaks.

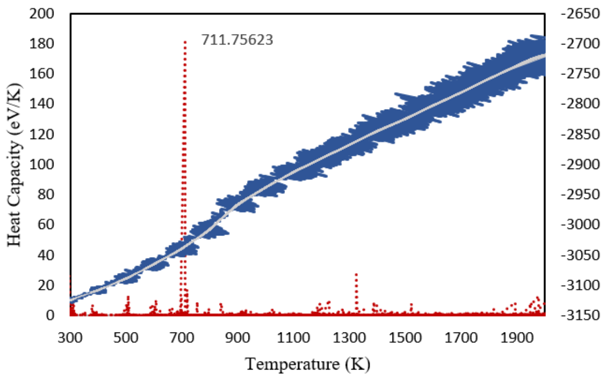

Figure 5-17: The potential energy (blue and silver) and the heat capacity (red) curves for pure aluminum.

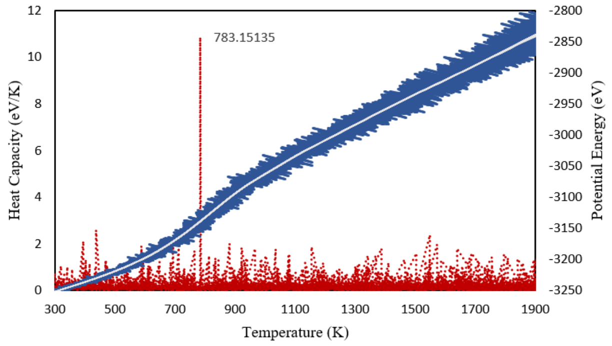

Figure 5-18: The potential energy (blue and silver) and the heat capacity (red) curves for Ti_1Al_9.

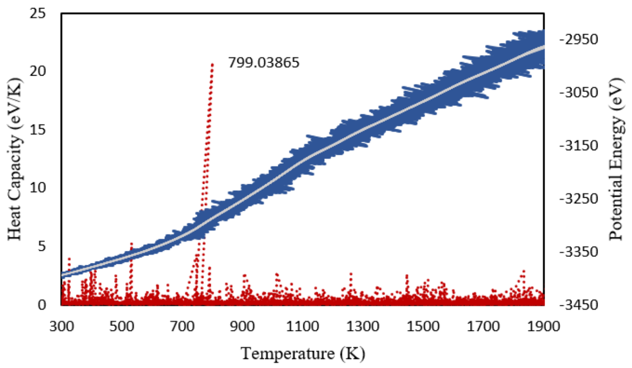

Figure 5-19: The potential energy (blue and silver) and the heat capacity (red) curves for Ti_2Al_8.

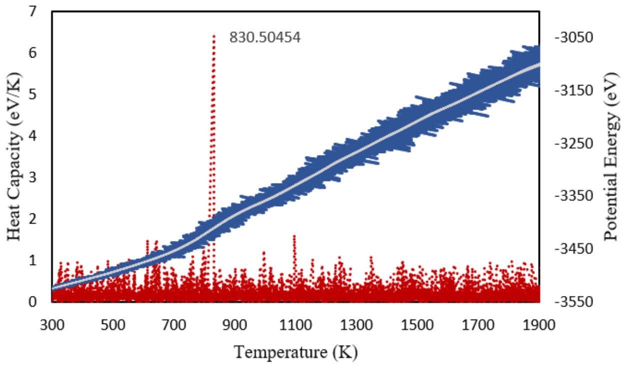

Figure 5-20: The potential energy (blue and silver) and the heat capacity (red) curves for Ti_3Al_7.

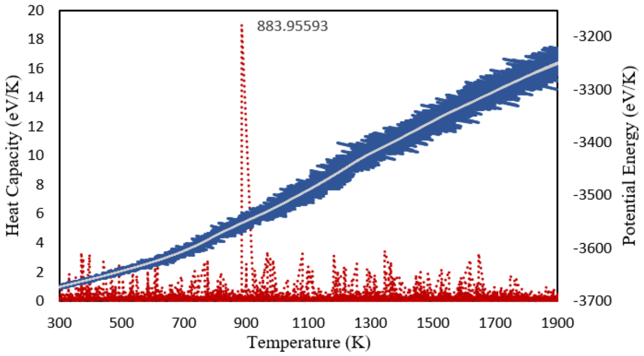

Figure 5-21: The potential energy (blue and silver) and the heat capacity (red) curves for Ti_4Al_6.

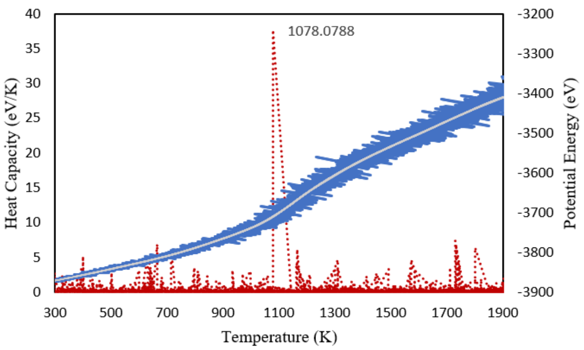

Figure 5-22: The potential energy (blue and silver) and the heat capacity (red) curves for Ti_5Al_5

.

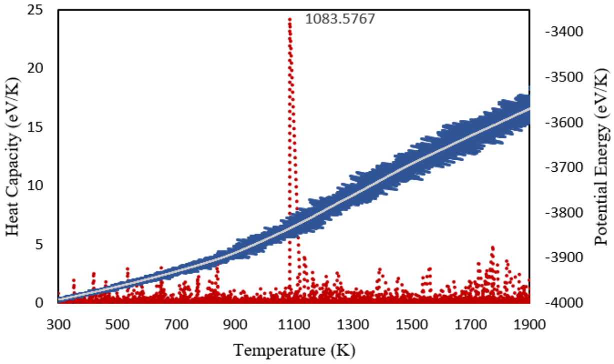

Figure 5-23: The potential energy (blue and silver) and the heat capacity (red) curves for Ti_6Al_4.

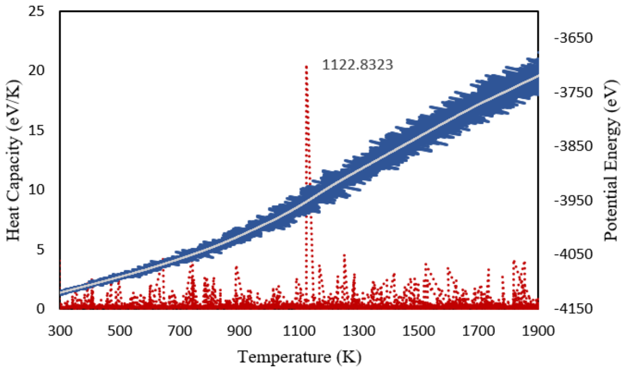

Figure 5-24: The potential energy (blue and silver) and the heat capacity (red) curves for Ti_7Al_3.

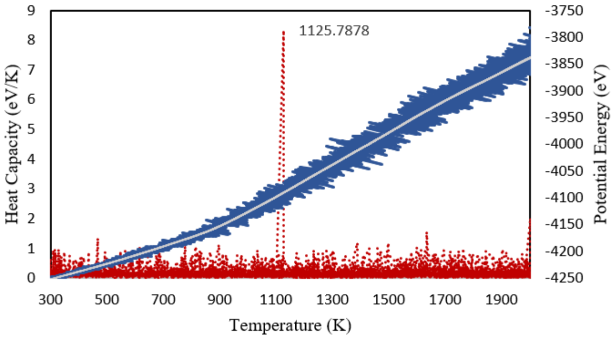

Figure 5-25: The potential energy (blue and silver) and the heat capacity (red) curves for Ti_8Al_2.

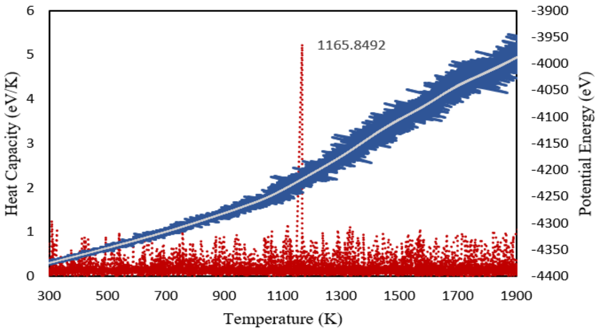

Figure 5-26: The potential energy (blue and silver) and the heat capacity (red) curves for Ti_9Al_1.

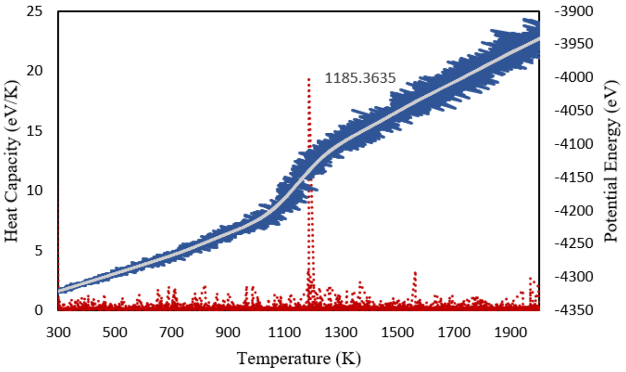

Figure 5-27: The potential energy (blue and silver) and the heat capacity (red) curves for pure titanium.

The blue lines represent the potential energy data which is noisy, and the red dotted lines represent the heat capacity curves obtained directly from the simulation. The silver line represents the noise reduced potential energy curves obtained from the Origin Pro software.

$$C_v = \left(\frac{\partial U}{\partial T}\right)_v \qquad \textbf{Eq. 5-1}$$

The heat capacity is the derivative of the potential energy with respect to the temperature **(Eq.5-1).** Hence, a peak on the heat capacity curve suggests a change in the slope which could mean that there is a phase change. From Figure 5-9, for pure aluminum, heat capacity peak is visible at 711.76K suggesting the phase change in pure aluminum has started at that temperature. At this temperature the cluster could be a mix of liquid and solid phases.

By analyzing this the melting temperatures of all the clusters are identified as follows:

Table 5-1: The melting temperatues of all cluster models obtained using the MEAM potential

Cluster	**Melting Temperature**
Pure titanium	711.76K
Ti_1Al_9	783.15K
Ti_2Al_8	799.04K
Ti_3Al_7	830.50K
Ti_4Al_6	883.96K
Ti_5Al_5	1078.09K
Ti_6Al_4	1083.58K
Ti_7Al_3	1122.83K
Ti_8Al_2	1125.79K
Ti_9Al_1	1165.85K
Pure titanium	1185.36K

In the MD study of melting of aluminum nanoparticles done by Alavi *et al.* [117], the melting temperature of a pure aluminum cluster of 1000 atom is reported to be about 620 K which is about 91 K less than this calculation. The authors use Strietz-Mintmire [118] electrostatic plus potential in that study. Due to the high surface to volume ratio, the melting temperatures of nanoparticles is significantly lower than their bulk counterparts. Considering that the bulk melting temperature of pure aluminum is around 933K, the results obtained in this study seem reasonable. Moreover, upon increasing the concentration of titanium in the systems, the melting temperatures has increased linearly.

CHAPTER 6

RESULTS AND DISCUSSION: EFFECTS OF CLUSTER SIZE ON SEGREGATION

6.1 Introduction

In the previous chapters, the structural changes and segregation studies of same sized nanoclusters with different compositions are done. In this study, the size effect on the segregation and structural evolution is studied using the timestep of 1 fs, the equilibration time of 100 ps, and the total simulation time of 1 ns. The initial clusters are modeled in Material's Studio. For this case, the composition of ~90 at% titanium and ~10 at% of aluminum is chosen for the nanoclusters of two different sizes. The first cluster has 1000 atoms with 900 titanium and 100 aluminum and the diameter of about 3.4 nm, whereas the second cluster has 10000 atoms with 9000 titanium and 1000 aluminum and the diameter of about 6.8 nm, therefore, the small cluster is named $Ti_{900}Al_{100}$ and the larger cluster is $Ti_{9000}Al_{1000}$ in this study. Similar to the previous study, the clusters were melted at 2500K and solidified at 300K, using both EAM and MEAM potentials. The simulation is conducted in LAMMPS and the cooling rate for this study is calculated to be $1.1x10^{12}$ K/s. **Figure 6-1** represents the 3.4 nm and 6.8 nm clusters obtained from Materials Studio software.

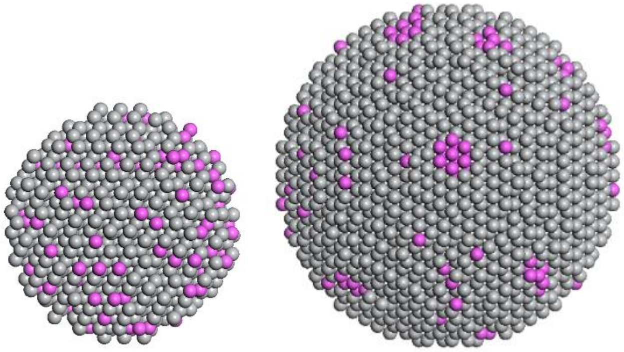

(a) (b)

Figure 6-1: The initial input clusters (a) 3.4 nm and (b) 6.8 nm in diameter obtained from Material's Studio software, Gray: titanium, Pink: aluminum

6.2 Results and Discussion

6.2.1 Structural Evolution

In this section, the structural transformation of both clusters is discussed. **Figure 6-2 - Figure 6-5** show the 3.4 nm EAM clusters, 3.4 nm MEAM clusters, 6.8 nm EAM clusters, and 6.8 nm MEAM clusters at different temperatures as they solidify to room temperature.

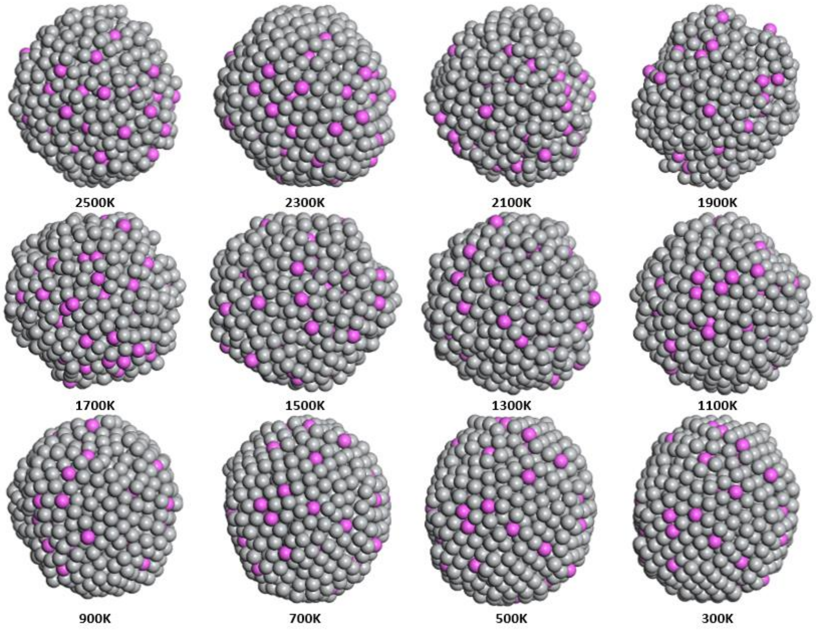

Figure 6-2: The evolution of the 3.4 nm ($Ti_{900}Al_{100}$) clusters from liquid to solid using the EAM potential.

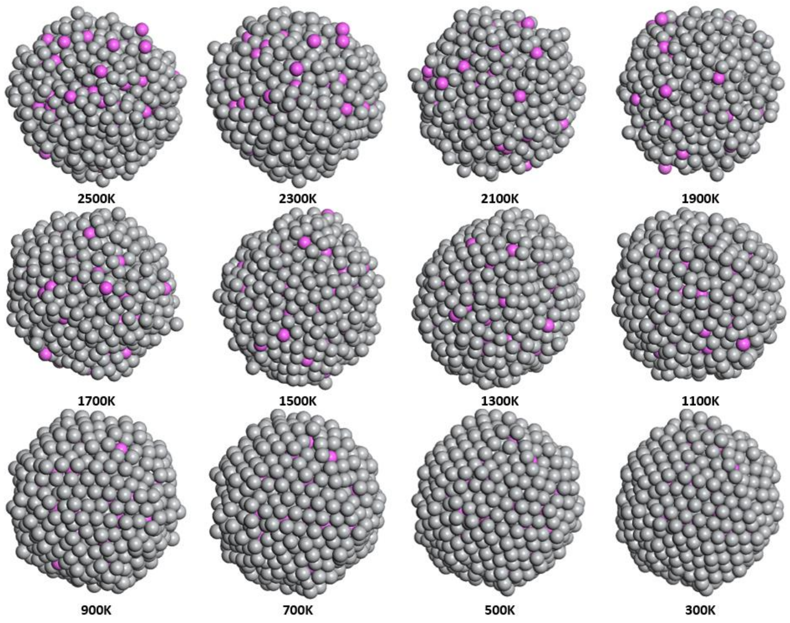

Figure 6-3: The evolution of the 3.4 nm ($Ti_{900}Al_{100}$) clusters from liquid solid using the MEAM potential.

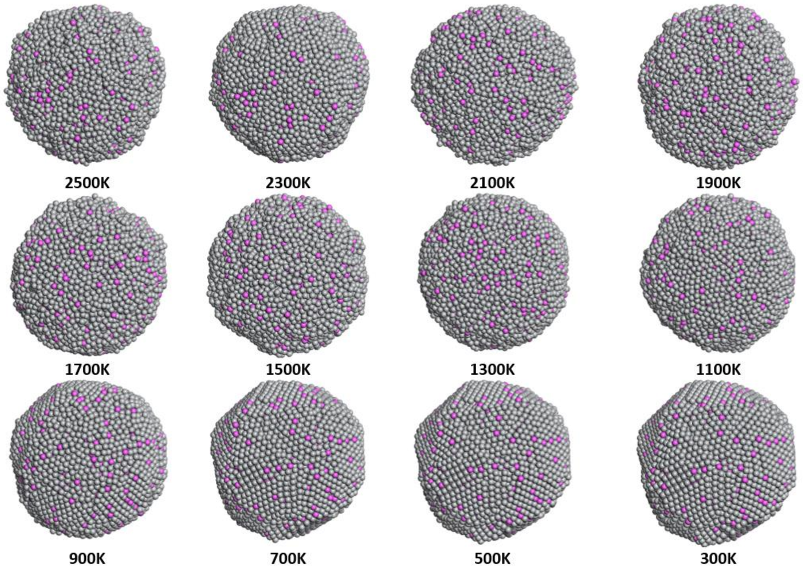

Figure 6-4: The evolution of the 6.8 nm ($Ti_{9000}Al_{1000}$) clusters from liquid solid using the EAM potential.

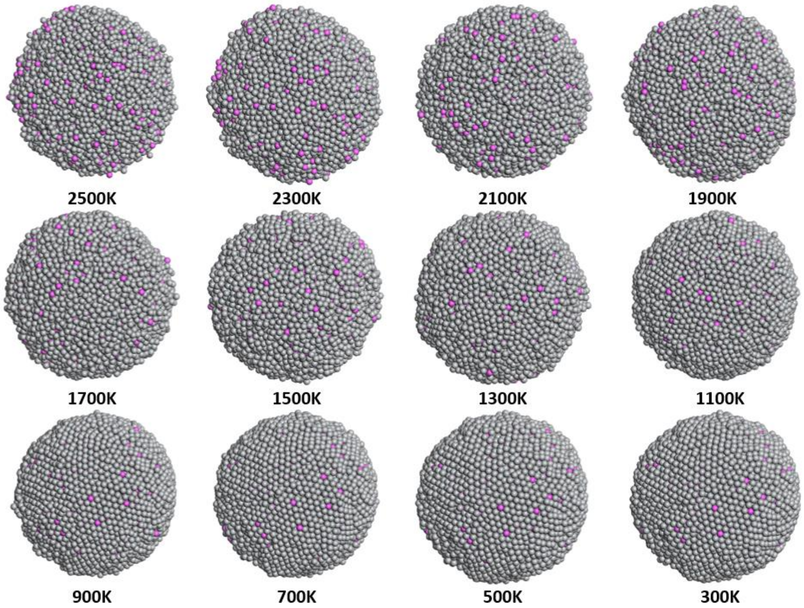

Figure 6-5: The evolution of the 6.8 nm ($Ti_{9000}Al_{1000}$) clusters from liquid solid using the MEAM potential.

The solidified surface structure of the 3.4 nm and the 6.8 nm EAM clusters containing 1000 and 10000 atoms respectively show that at both liquid and solidified state there are aluminum atoms present, whereas the solidified surface structure of the 3.4 nm and the 6.8 nm MEAM clusters show that the aluminum atoms are present in the liquid state but upon solidification the aluminum atoms are barely visible on the surface. Additionally, the solidified EAM clusters (both size) are clearly faceted. However, the solidified MEAM clusters have some atomic ordering but not clear faceting. From the previous study it is known that the titanium-rich clusters when the EAM potential is used, shows a probable icosahedral geometry. Likewise, in this study the EAM clusters (both size) tends to show an inclination to icosahedron at solidified state. The perfect icosahedron symmetry in these clusters is not visible, however, the facets are highlighted in yellow in **Figure 6-6** for visualization. This suggests that the atoms have started to nucleate. Depending on the cooling rate, metallic liquids can form either non-equilibrium phase or equilibrium phase upon solidification. The cooling rate used in this study makes this simulation the case of rapid cooling. Therefore, it can be concluded that if the cooling rate of the simulation is reduced to significantly lower magnitudes (10^5-10^7 K/s), the nucleation can be more pronounced and the MEAM potential eventually could predict this better.

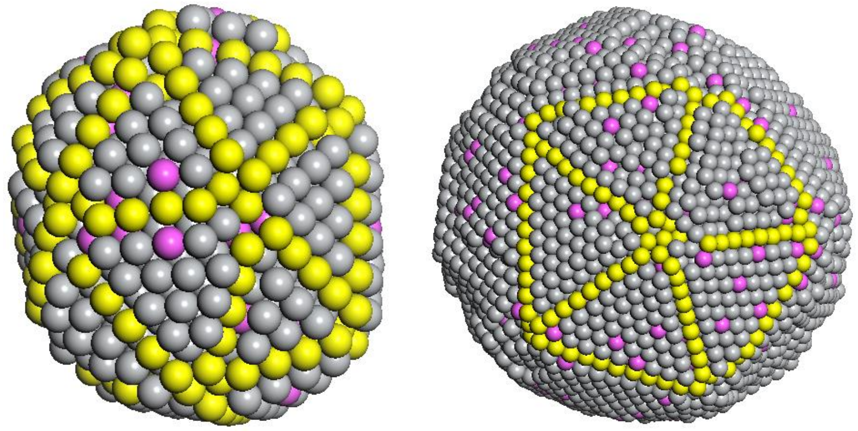

Figure 6-6: The solidified (a) $Ti_{900}Al_{100}$ and (b) $Ti_{9000}Al_{1000}$ clusters obtained using the EAM potential; yellow highlighted atoms for the visualization of facets.

6.2.2 Atom Segregation

This section discusses the atom density distribution obtained using the Eq. 4-1 and the effects on segregation when the size of the cluster is increased. The segregation is better explained in the following plots **(Figure 6-7 and Figure 6-8).**

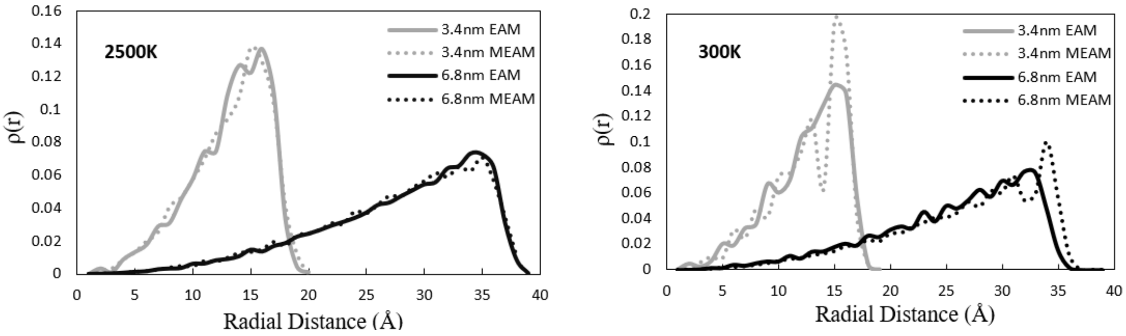

(a) (b)

Figure 6-7: The atomic radial density distribution of titanium atoms in both 3.4 nm and 6.8 nm clusters obtained using both EAM and MEAM potentials at (a) 2500K and (b) 300K.

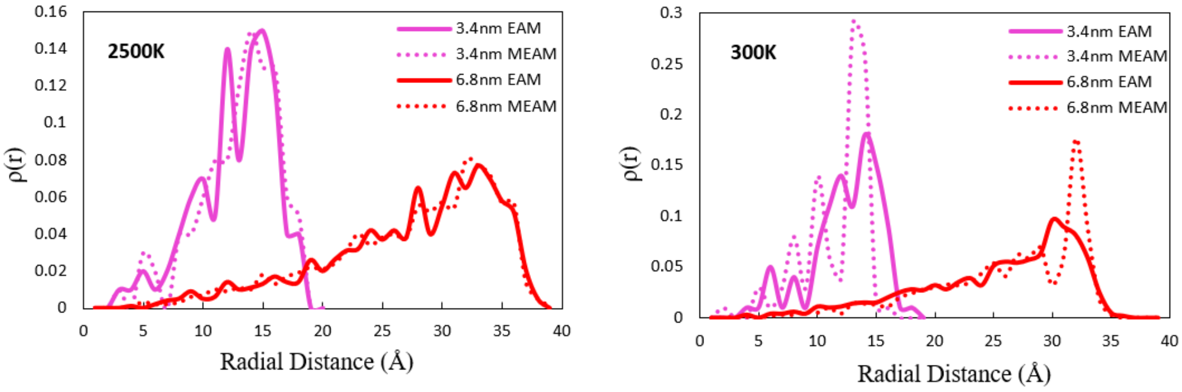

(a) (b)

Figure 6-8: The atomic radial density distribution of aluminum atoms in both 3.4 nm and 6.8 nm clusters obtained using both EAM and MEAM potentials at (a) 2500K and (b) 300K.

In Figure 6-7 and Figure 6-8, the grey and black lines represent titanium, the pink and red lines represent aluminum, the straight lines represent the results obtained from EAM potential, and the dotted lines represent the results from MEAM potential. From the atomic radial density distribution (Figure 6-7), in the melted EAM models, the higher concentration of titanium can be seen at the radial distance of 15-16Å for the 3.4 nm cluster and at 30-33Å for the larger cluster. The melted MEAM clusters also show the higher concentration of titanium at the same region as the EAM models. Upon solidification, the higher concentration of titanium for the small cluster is observed at 15-16Å and at 30-32Å for the larger clusters, in both potential models. The MEAM model also shows the concentration of titanium at the same radial distance for the smaller cluster, however, for the larger cluster, the higher concentration is shifted all the way to the surface. From Figure 6-8, for aluminum, in both the melted potential models, the highest concentration of aluminum is observed at the radial distance of 12-15Å for the smaller clusters. For the larger clusters, both EAM and MEAM melted clusters show the highest concentration of aluminum at the radial distance of 31-33Å. The solidified EAM clusters show that the aluminum concentrates at the radial distance of 15Å for the smaller and at 30Å for the larger cluster. The solidified MEAM clusters show that the aluminum concentrates at the distance of 12-14Å for the smaller and at 31-33Å for the larger cluster.

The multiple distinct peaks obtained from the MEAM models (titanium and aluminum) suggest that some kind of atomic ordering is being formed at those radial distances. This could also mean that the MEAM potential has better resolution than the EAM potential. Therefore, the segregation of aluminum in the surface region is prevalent at the liquid and solid state using either of the forcefields. The cause for such segregation could be the large difference between the melting temperatures of the alloying elements (titanium and aluminum).

6.2.3 Potential Energy and Heat Capacity Curves

Figure 6-9 – Figure 6-12 represent the temperature vs potential energy and heat capacity curves for both clusters using both forcefields.

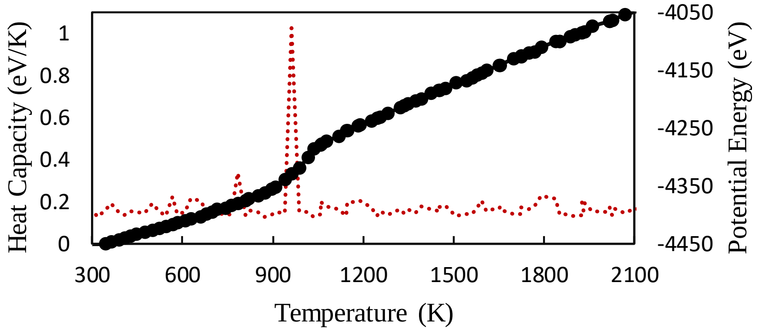

Figure 6-9: The potential energy (black) and the heat capacity (red) curves for the 3.4 nm ($Ti_{900}Al_{100}$) cluster obtained using the EAM potential.

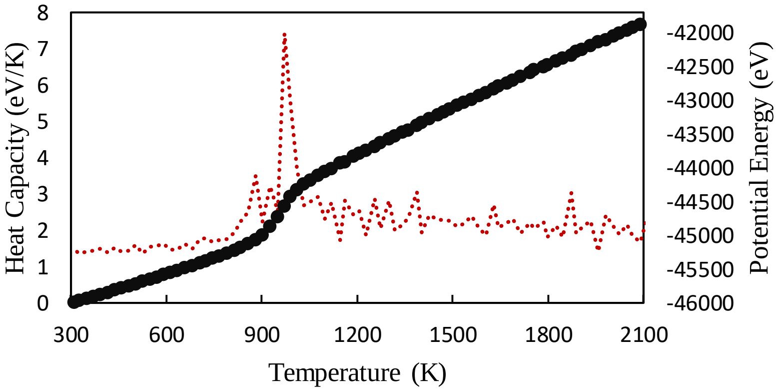

Figure 6-10: The potential energy (black) and the heat capacity (red) curves for the 6.8 nm ($Ti_{9000}Al_{1000}$) cluster obtained using the EAM potential.

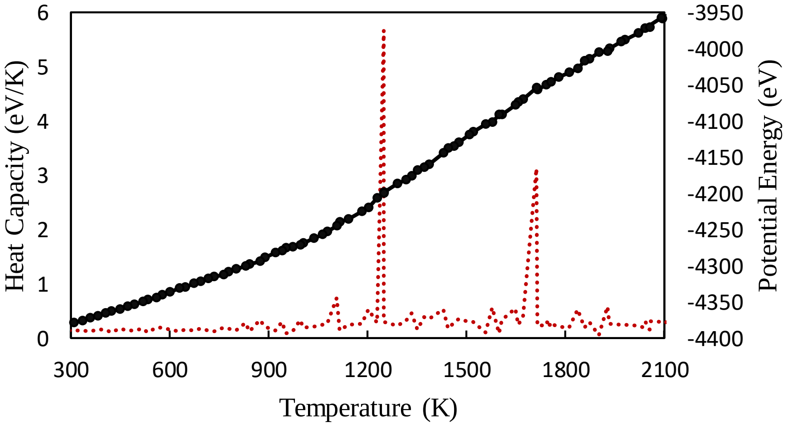

Figure 6-11: The potential energy (black) and the heat capacity (red) curves for the 3.4 nm ($Ti_{900}Al_{100}$) cluster obtained using the MEAM potential.

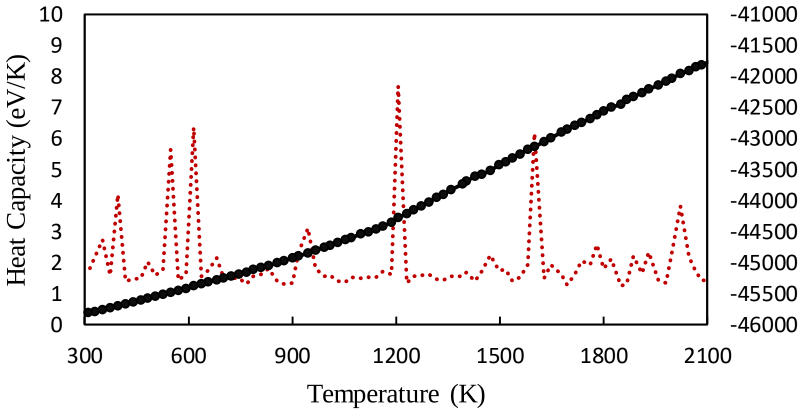

Figure 6-12: The potential energy (black) and the heat capacity (red) curves for the 6.8 nm ($Ti_{9000}Al_{1000}$) cluster obtained using the MEAM potential.

Figure 6-9 and Figure 6-10 are the potential energy and heat capacity curves for the 3.4 nm and 6.8 nm EAM clusters respectively. A distinct change in slope of the potential energy curve is visible in both cases. The heat capacity curve sensed the change at 962.5K for the smaller cluster and at 971.8K for the larger cluster. The melting temperatures did not significantly change for the larger system. The potential energy and the heat capacity curves obtained from the MEAM potential for both cluster sizes are shown in Figure 6-11 and Figure 6-12. There can be seen no distinct change in slope in the potential energy curve however, small transitions were sensed by the heat capacity curves. The multiple heat capacity peaks could simply be from the noise of the data or it could mean that the MEAM potential could be predicting some other phases at those temperatures where a peak is observed. Also, depending on the temperature different phases can be observed in an alloy. In the case of MEAM models, some transitions may be being seen as the solidification proceeds. The sharp peaks at around 1200K might mean that the melting started around that temperature. If this is the case, it contradicts the observation from the EAM potentials. Further precise melting temperature calculations and analysis is needed to shed light in this situation.

CHAPTER 7

CONCLUSION AND FUTURE WORKS

7.1 Conclusions

In this thesis, the behavior of titanium-aluminum bimetallic nanoparticles upon the heat treatment is studied utilizing the molecular dynamics simulations with two different forcefields. Several conclusions are drawn from this study and are summarized here:

- Our calculations show that both EAM and MEAM potentials predict segregation of aluminum in liquid and solid states. However, in the cases of high titanium content MEAM models (Ti_7Al_3, Ti_8Al_2, and Ti_9Al_1), aluminum migrates to the surface of the cluster at solid state but not in the liquid state.
- The titanium-rich MEAM models (Ti_7Al_3, Ti_8Al_2, ad Ti_9Al_1) show low segregation of aluminum and therefore should be further explored for SLM powder creation for better adhesion between the interfacial layers. Aluminum is not preferred on the surface upon solidification because if that is the case, considering the weak aluminum-aluminum bond strength, the adhesion between the two interfacial layers becomes very weak, reducing the overall strength of the 3D printed part.
- The EAM potential produces distinct solid structures (icosahedron) with visible facets in the titanium rich cluster models (Ti_8Al_2, Ti_9Al_1, pure titanium)

- The MEAM potential produces distinct solid structures (truncated octahedron) for aluminum-rich cluster models (pure aluminum, Ti_1Al_9, Ti_2Al_8).
- In the size effect study in chapter 6, the EAM models show one distinct heat capacity peak at 962.5K for the smaller cluster (3.4 nm, $Ti_{900}Al_{100}$) and at 971.8K for the larger cluster (6.8 nm, $Ti_{9000}Al_{1000}$) suggesting that the phase change starts at that temperature for those titanium-rich clusters. However, the MEAM models predicted multiple peaks in the heat capacity curve in both clusters. The most intense peak representing the significant phase change is observed at ~1200K in both clusters. This could mean that MEAM predicted small phase changes in the system and may have better resolution than the EAM potential.
- It is observed that the phase transition temperature, structural evolution, and segregation do not depend on the cluster size.

7.2 Future Work

- The metal systems start to exhibit bulk properties at the scale of 10^4 and higher. In this thesis the atom systems of 10^3 and 10^4 is used. The future work will be to start with multiscale simulation at the system size higher than 10^4 to resemble more macroscopic models.
- In real SLM environment, pressure plays an important role. Therefore, inclusion of the pressure parameters in the simulations will be more realistic.
- By the end of the study, the importance of the influence of cooling rate in the microstructure is realized. Faster cooling rates cause little time for crystal formation so amorphous structures can be observed whereas, slower cooling rate provides longer incubation time for the atoms and have more chances to occupy

the low energy position forming the crystals. Therefore, comparative simulation studies under different cooling rates will give an insight into the atomic ordering better.

- Exploring the mechanical properties of the systems could be useful in characterizing better metal powders for 3D printing applications.
- Currently, the mostly used metal powder for SLM is Ti-6Al-4V. However, computer simulation in this ternary composition of titanium-aluminum-vanadium is not possible because of the unavailability of forcefield for such system. Upon availability of the forcefield for this system, further investigation on segregation, mechanical properties, thermal stability, and structural evolution can be done.

APPENDIX A

PBS SCRIPT WRITTEN FOR RUNNING THE SIMULATIONS IN CERBERUS SUPERCOMPUTER

```
#!/bin/bash
#
# Batch queue to use
#PBS -q workq
#
# Requested number of nodes, cores per node, and wall-clock time (HH:MM:SS)
#PBS -l nodes=4:ppn=2
#PBS -l walltime=144:00:00
#
# Name of the job and the standard output/error files (merge with '-j oe')
#PBS -N <Name_of_the_job>
#PBS -j oe
#PBS -o par.out
#PBS -e par.err
cd $PBS_O_WORKDIR
#./<Name_of_file.py>  >log
exit
```

APPENDIX B

PYTHON CODE WRITTEN FOR CONVERTING EXCEL COORDINATE FILE FROM MATERIALS STUDIO TO .XYZ FORMAT

```
import xlrd
import os
from ase import Atom
from ase import Atoms
from ase.calculators.emt import EMT
from ase.optimize import BFGS
import numpy as np
from ase.io import write
# Go to the location of your Excel file and look at the location bar.
# To add add a directory in the file_location, simply insert another directory name
in single quotes and separated by commas.
file_location = os.path.join(os.path.expanduser('~'), '<Filename>.xlsx')
workbook = xlrd.open_workbook(file_location)
# WORKBOOK SHEET
# The first sheet in a workbook is specified as 0.
# The second is 1, etc.
sheet = workbook.sheet_by_index(0)
sata=[[sheet.cell_value(r, c) for c in range(sheet.ncols)] for r in
range(sheet.nrows)]
# CONVERSION CODE
data=np.array(sata)
x=[]
y=[]
z=[]
n=[]
coordinates=[]
Coordinates=[]
Element=[]
a=[]
L=(data[:,7])
for i in range(len(sata)):
```

```
    x.append(sata[i][1])
    y.append(sata[i][2])
    z.append(sata[i][3])
for i in range(len(x)):
    coordinates.append(x[i])
    coordinates.append(y[i])
    coordinates.append(z[i])
Coordinates.append(np.array(coordinates).reshape(-1,3))
#print (Coordinates)
for i in range(len(L)):
    Element.append(str(L[i]))
    #Element.append(Coordinates[0][i])
    #print (Element[i], Coordinates[0][i])
#print (Element)
for i in range(len(Element)):
    A = (Atom(Element[i], Coordinates[0][i]))
    a.append(A)
# PRINT
# This is the finished converted file to be used in the Simulation code.
# You can specify what to name the converted file here.
print (a)
molecule=Atoms(a)
write('<Filename>.xyz' , molecule
```

APPENDIX C

ASE CODE FOR MINIMA HOPPING

```
from ase import Atom
from ase import Atoms, io, optimize
from ase.calculators.eam import EAM
from ase.optimize import BFGS
import numpy as np
from ase.io import write, read
from ase.optimize.minimahopping import MinimaHopping
from ase.data import chemical_symbols
from ase.constraints import FixAtoms
# CONVERTED FILE NAME INPUT
# Change this to the converted file name. (Found at the bottom of the Converter code under the PRINT section.)
fName= <Filename>.xyz'
struct = read(fName)
constraints= [FixAtoms(mask=[a.symbol=='Ti' for a in struct])]
struct.set_constraint(constraints)
calc= EAM(potential=’<Potential_Library>’)
struct.set_calculator(calc)
#opt=BFGS(struct)
#opt.run(fmax=0.02)
#write('fName.xyz', struct)
e_struct = struct.get_potential_energy()
print('cluster molecule energy: %5.2f eV' % e_struct)
# Instantiate and run the minima hopping algorithm.
hop = MinimaHopping(struct, Ediff0=2.5, T0=2000, optimizer=BFGS)
hop(totalsteps=20)
from ase.optimize.minimahopping import MHPlot
mhplot = MHPlot()
mhplot.save_figure('summary.png')
```

BIBLIOGRAPHY

[1] I. Gibson, D. W. Rosen and B. Stucker, Additive Manufacturing Technologies: Rapid Prototyping to Direct Digital Manufacturing, London: Springer, 2010.

[2] I. Anderson, E. M. White and R. Dehoff, "Feedstock powder processing research needs for additive manufacturing development," *Current Opinion in Solid State and Materials Science,* vol. 22, no. 1, pp. 8-15, 2018.

[3] "ASTM F2792-12a, Standard Terminology for Additive Manufacturing Technologies," in *ASTM International*, West Conshohocken, PA, 2012.

[4] C. W. Hull, "Apparatus for production of three-dimensional objects by stereolithography". US Patent US4575330 A, 11 March 1986.

[5] C. K. Chua, K. F. Leong and C. S. Lim, Rapid prototyping: principles and applications., River Edge, NJ: World Scientific Publishing Co, 2010.

[6] K. Takahashi and J. Setoyama, "A UV-exposure system using DMD," *Electronics and Communication in Japan,* vol. 83, no. 7, pp. 56-58, 2000.

[7] S. Maruo, O. Nakamura and S. Kawata, "Three-dimensional microfabrication with two-photon absorbed photopolymerization," *Optics Letters,* vol. 22, no. 2, pp. 132-134, 1997.

[8] F. P. Melchels, J. Feijen and G. W. Grijpma, "A review on stereolithography and its applications in biomedical engineering," *Biomaterials,* vol. 31, no. 24, pp. 6121-6130, 2010.

[9] D. Bak, "Rapid prototyping or rapid production? 3D printing processes move industry towards the latter," *Assembly Automation,* vol. 23, no. 4, pp. 340-345, 2003.

[10] B. d. Gans, P. C. Duinevald and U. S. Schubert, "Inkjet printing of polymers: state of the art and future developments," *Advanced Materials,* vol. 16, no. 3, pp. 203-213, 2004.

[11] B. King and M. Renn, "Aerosol Jet Direct Write Printing for Mil-Aero Electronic Applications," Lockheed Martin, Palo Alto Colloquia, 2009.

[12] B. Derby and N. Reis, "Inkjet Printing of Highly Loaded Particulate Suspensions," *MRS Bulletin,* vol. 28, no. 11, pp. 815-818, 2003.

[13] W. Cao and Y. Miyamoto, "Freeform fabrication of aluminum parts by direct deposition of molten aluminum," *Journal of Materials Processing Technology,* vol. 173, no. 2, pp. 209-212, 2006.

[14] B. Stucker, "Additive manufacturing technologies: technology introduction and business implications," *Frontiers ofr Engineering: Reports on Leading-Edge Engineering,* pp. 5-14, 2011.

[15] J. H. Chun, C. H. Passow and N. P. Suh, "Droplet-Based Manufacturing," *CIRP Annual- Manufacturing Technology,* vol. 42, no. 1, pp. 235-238, 1993.

[16] C. A. Chen, J. H. Chun and G. Sohlenius, "Development of a Droplet-Based Manufacturing Process for Free Form Fabrication," *CIRP Annual-Manufcaturing Technology,* vol. 46, no. 1, pp. 131-134, 1997.

[17] T. T. Wohlers, "Additive Manufacturing and 3D Printing State of the Industry," Annual Worldwide Progress Report, 2013.

[18] S. S. Crump, "Apparatus and method for creating three-dimensional objects". US Patent US5121329, 9 June 1992.

[19] M. L. Novakova, M. J. Novak, J. Barna and J. Torok, "Special materials used in FDM rapid prototyping technology application," in *IEEE 16th International Conference on Intelligent Engineering Systems*, 2012.

[20] C. S. Marchi, M. Kouzeli, R. Rao, J. A. Lewis and D. C. Dunand, "Alumina-aluminum interpenetrating=phase composites with three-dimensional periodic architecture," *Scripta Materilia,* vol. 49, no. 9, pp. 861-866, 2003.

[21] M. A. Jafari, W. Han, F. Mohammadi, A. Safari, S. C. Danforth and N. Langrana, "A novel system for fused deposition of advanced multiple ceramics," *Rapid Prototyping Journal,* vol. 6, no. 3, pp. 161-175, 2000.

[22] S. H. Masood and W. Q. Song, "Development of new metal/polymer materials for rapid tooling using fused deposition modeling," *Materials and Design,* vol. 25, no. 7, pp. 587-594, 2004.

[23] J. Lipton, D. Arnold, F. Nigl, N. Lopez, D. L. Cohen, N. Noren and H. Lipson, *Multi-material food printing with complex internl structure suitable for conventional post-processing,* 2010.

[24] M. S. Kim, W. S. Chu, Y. M. Kim, A. P. Avila and S. H. Ahn, "Direct metal printing of 3D electrical circuit using rapid prototyping," *International Journal of Precision Engineering and Manufacturing,* vol. 10, no. 5, pp. 147-150, 2009.

[25] M. Feygin, "Apparatus and method for forming an integral object from laminations". US Patent US5354414A, 5 October 1988.

[26] E. Sachs, M. Cima, P. Williams, D. Brancazio and J. Cornie, "Three dimensional printing: rapid tooling and prototypes directly from a CAD model," *Journal of Engineering for Industry,* vol. 114, no. 4, pp. 481-488, 1992.

[27] M. Chhabra and R. Singh, "Rapid casting solutions: a review," *Rapid Prototyping Journal,* vol. 17, no. 5, pp. 328-350, 2011.

[28] M. Stankiewicz, G. Budzik, M. Patrza, M. Wieczorowski, M. Grzelka, H. Matysiak and J. Slota, "The scope of application of incremental rapid prototyping methods in foundry engineering," *Archives of Foundry Engineering,* vol. 10, no. 1, pp. 405-410, 2010.

[29] K. V. Wong and A. Hernandez, "A Review of Additive Manufacturing," *ISRN Mechanical Engineering,* pp. 1-10, 2012.

[30] D. W. Lipke, Y. Zhang, B. Liu, B. C. Church and K. H. Sandhage, "Near net-shape/net-dimension ZrC/W-based composites with complex geometries via rapid prototyping and Displacive Compensation of Porosity," *Journal of Eueopean Ceramics Scociety,* vol. 30, no. 11, pp. 2265-2277, 2010.

[31] W. U. Syed, A. J. Pinkerton and L. Li, "A comparative study of wire feeding and powder feeding in direct diode laser deposition for rapid prototyping," *Applications of Surface Science,* vol. 247, no. 1, pp. 344-348, 2005.

[32] R. M. Miranda, G. Lopes, L. Quintino, J. P. Rodrigues and S. Williams , "Rapid prototyping with high power fiber lasers," *Materials and Design,* vol. 29, no. 10, pp. 2072-2074, 2008.

[33] K. M. Taminger and R. A. Hafley, "Electron beam freeform fabrication: a rapid metal deposition process," in *Proceedings of 3rd Annual Automotive Composites Conference*, 2003.

[34] K. M. Martina, J. Mehnen, S. Williams, P. Colegrove and F. Wang, "Investigation of the benefits of plasma deposition for the additive layer manufacture of Ti-6Al-

4V," *Journal of Materials Processing Technology,* vol. 212, no. 6, pp. 1377-1386, 2012.

[35] G. P. Dinda, A. K. Dasgupta and J. Mazumder, "Laser aided direct metal deposition of Inconel 625 superalloy: Microstructural evolution and thermal stability," *Materials Science Engineering,* vol. 509, no. 1, pp. 98-104, 2009.

[36] J. J. Beaman and C. R. Deckard, "Selective laser sintering with assisted powder handling". US Patent US4938816 A, 30 July 1990.

[37] H. Tang, M.-L. Chiu and H.-C. Yen, "Slurry-Based Selective Laser Sintering of Polymer-Coated Ceramic Powders to Fabricate High Strength Alumina Parts," *Journal of the European Ceramic Society,* vol. 31, no. 8, pp. 1383-1388, 2011.

[38] M. Vaezi, H. Seitz and S. Yang, "A review on 3D micro-additive manufacturing technologies," *International Journal of Manufacturing Technology,* vol. 67, 2012.

[39] S. Bremen, W. Meiners and A. Diatlov, "Selective Laser Melting," *Laser Technik Journal,* vol. 9, no. 2, pp. 33-38, 2012.

[40] A. Gebhardt, F.-M. Schmidt, J.-S. Hotter, W. Sokalla and P. Sokalla, "Additive Manufacturing by Selective Laser Melting The Realizer Desktop Machine and its application for the Dental Industry," *Physics Procedia,* vol. 5, pp. 543-549, 2010.

[41] C. Y. Yap, L. E. Loh, S. L. Sing, Z. L. Dong, Z. H. Liu, D. Q. Zhang and C. K. Chua, "Review of selective laser melting: Materials and applications," *Applied Physics Reviews,* vol. 2, pp. 041101-041122, 2015.

[42] I. Yadroitsev and I. Smurov, "Surface Morphology in Selective Laser Melting of Metal Powders," *Physics Procedia,* vol. 12, pp. 264-270, 2011.

[43] T. B. Sercombe and X. Li, "Selective laser melting of aluminum and aluminum metal matrix composites: review," *Materials Technology,* vol. 31, no. 2, pp. 77-85, 2016.

[44] L. C. Zhang and H. Attar, "Selective Laser Melting of Titanium Alloys and Titanium Matrix Composites for BIomedical Applications," *Advanced Engineering Materials,* vol. 18, pp. 463-475, 2015.

[45] A. V. Agapovichev, V. V. Kokarena, V. G. Smelov and A. V. Sotov, "Selective laser melting of titanium alloys: investigation of mechanical properties and microstructure," *Materials Science and Engineering,* p. 156, 2016.

[46] X. Zhao, S. Li, M. Zhang, Y. Liu, T. B. Sercombe, S. Wang, Y. Hao, R. Yang and L. E. Murr, "Comparison of the microstructure and mechanical properties of Ti-

6Al-4V fabricated by selective laser melting and electron beam melting," *Materials and Design,* vol. 95, no. 5, pp. 21-31, 2016.

[47] W. D. Callister, Materials Science and Engineering: An Introduction, John Wiley and Sons Inc, 2007.

[48] Q. Pei, C. Lu and M. Fu, "The Rapid Solidification of Ti3Al: A Molecular Dynamics Study," *J Phys: Conden Matter,* vol. 16, pp. 4203-4210, 2004.

[49] B. Zhang, X. Zhang, C. Li and K. Zhou, "Molecular Dynamics Simulation on Phase Transformation of Ti-Al Alloy with Low Al Content," *Rare Metal Materials and Engineering,* vol. 41, no. 6, pp. 1010-1015, 2012.

[50] J. Slotwinski, E. Garbockzi, E. Stutzman, C. Ferraris, S. Watson and M. Peltz, "Characterization of Metal Powders Used for Additive Manufacturing," *Journal of Research of the National Institute of Standards and Technology,* vol. 119, pp. 460-493, 2014.

[51] I. Yamauchi, I. Ohnaka, S. Kawamoto and T. Fukusako, "Hot Extrusion of Rapidly Solidified Al-Si Alloy Powder by the Rotating-Water-Atomization Process," *Transactions of the Japan Institute of Metals,* vol. 27, no. 3, pp. 195-203, 1986.

[52] D. Hu and M. H. Loretto, "Microstructural characterization of a gas atomized Ti6Al4V-TiC composite," *Scripta Metallurgica et Materialia,* vol. 31, no. 5, pp. 90141-90145, 1994.

[53] R. Li, Y. Shi, Z. Wang, L. Wang, J. Liu and W. Jiang, "Densification behavior of gas and water atomized 316L stainless steel powder during selective laser melting," *Applied Surface Science,* vol. 256, no. 13, pp. 4350-4356, 2010.

[54] W. A. Kaysser and K. Rzesnitzek, "Principles of Atomization," in *Science of Sintering*, Boston, Springer, 1989, pp. 157-176.

[55] G. Yablokova, M. Speirs, J. V. Humbeeck, J. P. Kruth, J. Schrooten, R. Cloots and F. Boschini, "Rheological behavior of B-Ti and NiTi powders produced by atomization of SLM production of open porous orthopedic implants," *Powder Technology,* vol. 283, pp. 199-209, 2015.

[56] P. Sungkhaphaitoon, T. Plookphol and S. Wisutmethangoon, "Design and Development of a Centrifugal Atomizer for Producing Zinc Metal Powder," *International Journal of Applied Physics and Mathematics,* vol. 2, no. 2, pp. 77-82, 2012.

[57] N. Nomura, S. Yalatu, Y. Tsutsumi, T. Hanama, T. Nakamoto, T. Kimura, K. Kikuchi and A. Kawasaki, "Effect of powder fabrication process on microstructure and mechanical properties of selective laser melted metals for biomedical applications," in *10th World Biomaterials Congress*, 2016.

[58] V. Uhlenwinkel, L. Achelis, S. Sheikhaliev and S. Lagutkine, A new Technique for Molten Metal Atomization, Sorento, Italy: Proc. ICLASS, 2003.

[59] S. Dietrich, M. Wunderer , A. Huissel and M. F. Zaeh, "A New Approach For A Flexible Powder Production For Additive Manufacturing," *Procedia Manufacturing,* vol. 6, pp. 88-95, 2016.

[60] M. Simonelli, Y. Tse and C. Tuck, "The formation of a+b microstructure in as-fabricated selective laser melting of Ti-6Al-4V," *Journal of Materials Research,* vol. 29, pp. 2028-2035, 2014.

[61] E. Chlebus, B. Kuznicka, T. Kurzynowski and B. Dybala, "Micrsostructure and Mechanical Behavior of Ti-6Al-7Nb Alloy Produced by Selective Laser Melting," *Material Characterization,* vol. 62, pp. 488-495, 2011.

[62] C. Qiu, N. J. Adkins and M. M. Atallah, "Microstructure and tensile properties of selectively laser-melted and HIPed laser-melted Ti-6Al-4V," *Materials Science and Engineering: A,* vol. 578, pp. 230-239, 2013.

[63] P. Krakhmalev, G. Fredriksson, I. Yadroitsava, N. Kazantseva, A. d. Plessis and I. Yadroitsev, "Deformation behavior and microstructure of Ti6Al4V manufactured by SLM," *Physics Procedia,* vol. 83, pp. 778-788, 2016.

[64] A. E. Patterson, S. L. Messimer and P. A. Farrington, "Overhanging Features and the SLM/DMLS Residual Stresses Problem: Review and Future Research Need," *Additive Manufacturing Technologies and Applications,* vol. 5, no. 2, p. 15, 2017.

[65] C. R. Knowles, T. H. Becker and R. B. Tait, "Residual Stress Measurements and Structural INtegrity Implications for Selective Laser Melted Ti-6Al-4V," *South African Journal of Industrial Engineering,* vol. 23, pp. 119-129, 2012.

[66] J. p. Kruth, J. V. Vaerenbergh, L. Froyen and B. Lauwers, "Selective laser melting of iron-based powder," *Journal of Materials Processing Technology,* vol. 149, no. 1-3, pp. 616-622, 2004.

[67] S. Kolossov, E. Boillat, M. Locher, R. Glardon and P. Fischer, "3D FE simulation for temperature evolution in selective laser sintering process," *International Journal of Machine Tools and Manufacture,* vol. 44, no. 2, pp. 117-123, 2004.

[68] I. A. Roberts, R. Exterlein, C. J. Wang, D. Mynors and M. Stanford, "A three-dimensional finite element alanysis of the temperature field during laser melting of metal powders in additive layer manufacturing," *International Journal of Machine Tools and Manufacture,* vol. 49, no. 12, pp. 916-923, 2009.

[69] D. Q. Zhang, Q. Z. Cai, J. H. Liu, L. Zhang and R. D. Li, "Select laser melting of W-Ni-Fe powders: simulation and experimental study," *The International Journal of Advanced Manufacturing Technology,* vol. 51, no. 5, pp. 649-658, 2010.

[70] K. Zeng, D. Pal, N. Patil and B. Stucker, "A new dynamics mesh method applied to the simulation of Selective Laser Melting," in *24th International SFF Symposium - An Additive Manufacturing Conference*, Austin, 2013.

[71] J. T. Beals, Y. She, V. Jagdale and J. A. Sharon, "Structured Powder Particles for Feedstock Improvement for Laser Based Additive Manufacturing". United States Patent 20170368603A1, 28 December 2017.

[72] A. D. Brandao, R. Gerard, J. Gumpinger, S. Beretta, A. Makaya, L. Pambaguian and T. Ghidini, "Challenges in Additive Manufacturing of Spcae Parts: Powder Feedstock Cross-Contamination and Its Impact on End Products," *Materials,* vol. 10, no. 5, 2017.

[73] J. Ferrante and D. H. Buckley, "A Review of Surface Segregation, Adhesion and Friction Studies Performed on Copper-Aluminum, Copper-Tin and Iron-Aluminum Alloys," *A S L E Transactions,* vol. 15, no. 1, pp. 18-24, 1972.

[74] J. P. Kruth, M. Bradrossamy, E. Yasa, J. Deckers, L. Thijs and J. Van Humbeeck, "Part and material properties in selective laser melting of metals," in *Proceedings of the 16th International Symposium on Electromachining*, 2010.

[75] B. Wysocki, P. Maj, R. Sitek, J. Buhagiar, J. K. Kurzydłowski and W. Święszkowski , "Laser and Electron Beam Additive Manufacturing Methods of Fabricating Titanium Bone Implants," *Applied Sciences,* vol. 7, no. 7, pp. 657-677, 2017.

[76] S. Gorsse, C. Hutchinson, M. Goune and R. Banerjee, "Additive manufacturing of metals: a brief review of the characteristic microstructures and properties of steels, Ti-6Al-4V and high-entropy alloys," *Science and Technology of Advanced Materials,* vol. 18, no. 1, pp. 584-610, 2017.

[77] C. J. Bae, A. Ramachandranan and J. W. Halloran, "Quantifying particle segregation in sequential layers fabricated by additive manufacturing," *Journal of the European Ceramic Society,* p. in press, 2018.

[78] S. Haeri, Y. Yang, O. Ghita and J. Sun, "Discrete element simulation and experimental study of powder," *Powder Technologies,* vol. 306, pp. 45-54, 2017.

[79] L. Verlet and D. Levesque, "Molecular Dynamics and Time Reversibility," *Journal of Statistical Physics,* vol. 72, no. 3, pp. 519-537, 1993.

[80] A. Leach, Molecular Modelling: Principles and Applications, Pearson, 2001.

[81] R. L. Rowley, Y. Yang and T. A. Pakkanen, "Determination of an ethane intermolecular potential model for use in molecular simulations from ab initio calculations," *The Journal of Chemical Physics,* vol. 114, no. 4, pp. 6058-6067, 2001.

[82] F. H. Stillinger and T. A. Weber, "Computer simulation of local order in condensed phases of silicon," *Physical Review B,* vol. 31, no. 8, pp. 5262-5271, 1985.

[83] A. C. v. Duin, S. Dasgupta, F. Lorant and W. A. Goddard, "ReaxFF: A Reactive Force Field for Hydrocarbons," *The Journal of Physical Chemistry A,* vol. 105, no. 41, pp. 9396-9409, 2001.

[84] J. Tersoff, "Empirical interatomic potential for silicon with improved elastic properties," *Physical Review B,* vol. 38, no. 14, pp. 9902-9905, 1988.

[85] M. Daw and M. Baskes, "Embedded-Atom Method: Derivation and Application to Impurities, Surfaces, and Other Defects in Metals," *Physical Review B,* vol. 29, no. 12, pp. 6443-6453, 1984.

[86] M. I. Baskes, J. S. Nelson and A. F. Wright, "Semiempirical modified embedded-atom potentials for silicon and germanium," *Physical Review B,* vol. 40, no. 9, pp. 6085-6100, 1989.

[87] M. W. Finnis and J. E. Sinclair, "A simple empirical N-body potential for transition metals," *Philosophical Magazine A,* vol. 50, no. 1, pp. 45-55, 1984.

[88] F. Ercollesi and J. B. Adams, "Interatomic potential from first-principles calculation: the force-matching method," *Europhysics Letters,* vol. 26, no. 8, pp. 583-594, 1994.

[89] R. Zope and Y. Mishin, "Interatomic Potentials for Atomistic Simulations of the Ti-Al System," *Physical Review B,* vol. 68, no. 2, 2003.

[90] Y. Kim, H. Kim, W. Jung and B. Lee, "Atomistic Modeling of the Ti-Al Binary System," *Computational Materials Science,* vol. 119, pp. 1-8, 2016.

[91] M. I. Baskes, "Modified embedded-atom potentials for cubic materials and impurities," *Physical Review B,* vol. 46, no. 5, pp. 2727-2742, 1992.

[92] L. Byeong-Joo, K. Won-Seok, K. Hyun-Yun and K. Eun-Ha, "The modified embedded-atom method interatomic potentials and recent progress in atomistic simulations," *Calphad,* vol. 34, no. 4, pp. 510-522, 2010.

[93] M. I. Baskes and R. A. Johnson, "Modified embedded atom potentials for HCP metals," *Modeling and Simulation in Material Science and Engineering,* vol. 2, no. 1, p. 147, 1994.

[94] S. Shoutian, B. R. Ramachandranan and C. D. Wick, "Solid, liquid, and interfacial properties of TiAl alloys: parameterization of a new modified embedded atom method model," *Journal of Physics: Condensed Matter,* vol. 30, pp. 75002-75013, 2018.

[95] P. Debye, "Na¨herungsformeln fu¨r die Zylinderfunktionen fu¨r große Werte des Arguments und unbeschra¨nkt vera¨nderliche Werte des Index," *Mathematische Annalen,* vol. 67, pp. 535-558, 1909.

[96] M. R. Hestenes and E. Stiefel, "Methods of Conjugate Gradient for Solving Linear System," *Journal of Research of the National Bureau of Standards,* vol. 49, no. 6, pp. 409-436, 1952.

[97] T. J. Ypma, "Historical Development of the Newton-Raphson Method," *SIAM Review,* vol. 37, no. 4, pp. 531-551, 1995.

[98] D. C. Liu and J. Nocedal, "On the limited memory BFGS method for large scale optimization," *Mathematical Programming,* vol. 45, no. 1, pp. 503-528, 1989.

[99] L. Ying and L. Li, "Understanding the corrosion resistance of nanocrystalline materials: electrochemical influences," in *Corrosion Protection and Control Using Nanomaterials*, Woodhead Publishing, 2012, pp. 59-85.

[100] Z. C. Xie, T. H. Gao, X. T. Guo and Q. Xie , "Molecular dynamics simulation of nanocrystal formation and deformation behavior of Ti3Al alloy," *Computational Materials Science,* vol. 98, pp. 245-251, 2015.

[101] P. T. Li, Y. Q. Yang, W. Zhang, X. Luo, N. Jin and G. Liu, "Strcutural evolution of TiAl during rapid solidification processing revealed by molecular dynamics simulation," *RSC Advances,* vol. 6, pp. 54763-54768, 2016.

[102] J. Panova and D. Farkas, "Atomistic simulation of fracture in TiAl," *Metallurigical and Materials Transaction A,* vol. 29, no. 13, pp. 951-955, 1998.

[103] Y. Mishin and C. Herzig, "Diffusion in the Ti-Al system," *Acta Materialia*, vol. 48, no. 3, pp. 589-623, 2000.

[104] M. Shimono and H. Onodera, "Molecular Dynamics Study on Liquid-to-Amorphous Transition in Ti–Al Alloys," *Materials Transactions JIM*, vol. 39, no. 1, pp. 147-153, 1998.

[105] A. S. Lopis, Q. G. Reynolds and K. Bisaka, "Computational Simulation of Molten Titanium-Aluminum Metal and Alloys," Mintek, South Africa, 2010.

[106] W. Frazier, "Metal Additive Manufacturing: A Review," *Journal of Materials Engineering and Performance*, vol. 23, no. 6, pp. 1917-1928, 2014.

[107] D. Buchbinder, H. Schleifenbaum, S. Heidrich, W. Meiners and J. Bultmann, "High Power Selective Laser Melting (HP SLM) of Aluminum Parts," *Physics Procedia*, vol. 12, pp. 271-278, 2011.

[108] A. S. Lopis, Q. G. Reynolds and K. Bisaka, "Computational Simulation of Molten Titanium-Aluminum Metal and Alloys".

[109] Y. Jiang, Y. He, N. Xu, J. Zou, B. Huang and C. Liu, "Effect of the Al Content on Pore Structure of Porous Ti-Al Alloys," *Intermetallics*, vol. 16, pp. 327-332, 2008.

[110] R. Hennig, T. Lenosky, D. Trinkle, S. Rudin and J. Wilkins, "Classical potential describes martensitic phase transformations between the alpha, beta, and omega titanium phases," *Physical Review B*, vol. 78, no. 3, 2008.

[111] D. S. BIOVIA, *Materials Studio 6.0*, San Diego.

[112] S. Goedecker, "Minima Hopping: AN Efficient Search Method for the Global Minimum of teh Potential Energy Surface of Complex Molecular Systems," *J Chem Phys*, vol. 120, no. 21, pp. 9911-9917, 2004.

[113] S. R. Bahn and K. W. Jacobsen, "An object-oriented scripting interface to a legacy electronic structure code," *Computing in Science and Engineering*, vol. 4, no. 3, pp. 56-66, 2002.

[114] S. Plimton, "Fast Parallel Algorithms for Short-Range Molecular Dynamics," *Journal of Compuational Physics*, vol. 117, pp. 1-19, 1995.

[115] J. d. Laeter, J. K. Bohlke, P. d. Bievre, H. Hidaka, H. S. Reiser, K. R. Rosman and P. D. Taylor, "Atomic Weights of the Elements: Review 2000," *Pure Applied Chemistry*, vol. 75, no. 6, pp. 683-800, 2003.

[116] P. Hohenberg and W. Kohn, "Inhomogeneous Electron Gas," *Physical Review,* vol. 136, no. 3B, 1964.

[117] F. L. Tang, W. J. Lu, G. B. Chen, Y. Xie and W. Y. Yu, "Surface structure and solidification morphology of aluminum," *Physica B: Condensed Matter,* vol. 404, no. 16, pp. 2489-2494, 2009.

[118] M. Polak and L. Rubinovich, "The interplay of surface segregation and atomic order in alloys," *Surface Science Reports,* vol. 38, no. 4, pp. 127-194, 2000.

[119] S. Alavi and D. L. Thompson, "Molecular Dynamics Simulations of Melting of Aluminum Nanoparticles," *Journal of Physical Chemistry A,* vol. 110, no. 4, pp. 1518-1523, 2006.

[120] F. H. Streitz and J. W. Mintmire, "Electrostatic potentials for metal-oxide surfaces and interfaces," *Physical Review B,* vol. 50, no. 16, pp. 11996-12003, 1994.

[121] E. G. Noya and J. P. Doye, "Structural transitions in the 309-atom magic number Lennard-Jones cluster," *Journal of Chemical Physics,* vol. 124, no. 10, pp. 104503-104509, 2006.

[122] J. P. Kruth, M. C. Leu and T. Nakagawa, "Progress in Additive Manufacturing and Rapid Prototyping," *CIRP Annals,* vol. 47, no. 2, pp. 525-540, 1998.

[123] S. Saqib, R. J. Urbaine and K. Aggarwal, "Analysis of laser cladding bead morphology for developing additive manufacturing travel paths," *Procedia CIRP,* vol. 17, pp. 824-829, 2014.

[124] J. P. Kruth, P. Mercelis, J. V. Vaerenbergh, L. Froyen and M. Rombouts, "Binding mechanisms in selective laser sintering and selective laser melting," *Rapid Prototyping Journal,* vol. 11, no. 1, pp. 26-36, 2005.

[125] S. Bikas, P. Stavropoulos and G. Chryssolouris, "Additive manufacturing method and modelling approaches: a critical review," *International Journal of Advanced Manufacturing Technology,* vol. 83, pp. 389-405, 2015.

[126] M. Vaezi, S. Yang and B. G. Mellor, "Multiple Material Additive Manufacturing - Part 1: A Review," *Virtual and Physical Prototyping,* vol. 8, no. 1, pp. 19-50, 2013.

[127] K. V. Wong and A. Hernandez, "A Review of Additive Manufacturing," *ISRN Mechanical Engineering,* 2012.

[128] R. Noorani, Rapid Prototyping: Principles and Applications, Wiley, 2006.

[129] C. Duty, D. Jean and W. J. Lackey, "Laser chemical vapour deposition: materials modelling, and process control," *International Materials Review,* vol. 46, no. 6, pp. 271-287, 2001.

[130] C. C. Kai and L. K. Fai, Rapid Prototyping: Principles and Applications in Manufacturing, World Scientific Publishing Company, 2000.

[131] H. J. Berendsen, J. P. Postma, W. v. Gunsteren, A. Dinola and J. Haak, "Molecular dynamics with coupling to an external heat bath," *The Journal of Chemical Physics,* vol. 81, no. 8, pp. 3684-3690, 1984.

[132] K. Sangrak, "Issues on the choice of a Proper Time Step in Molecular Dynamics," *Physics Procedia,* vol. 53, pp. 60-62, 2014.

[133] F. H. Stillinger and A. Rahman, "Improved simulation of liquid water by molecular dynamics," *The Journal of Chemical Physics,* vol. 60, no. 4, p. 1545, 1974.

[134] K. Binder, J. Horbach, W. Kob, W. Paul and F. Varnik, "Molecular dynamics simulations," *Journal of Physics: Condensed Matter,* vol. 16, no. 5, pp. 429-453, 2004.

[135] D. Kosloff and R. Kosloff, "A Fourier Method Solution for the Time-Dependant Schrodinger Equation as a Tool in Molecular Dynamics," *Journal of Physcial Chemistry,* vol. 52, pp. 35-53, 1983.

[136] N. K. Tolochko, S. E. Mozzharov, I. A. Yadroitsev, T. Laoui, L. Froyen, V. I. Totov and M. B. Ignatiev, "Selective laser sintering and cladding of single-component metal powders," *Rapid Prototyping Journal,* vol. 10, no. 2, pp. 88-97, 2004.

[137] Z. Xie, T. Gao, T. Guo and Q. Xie, "Molecular Dynamics Simulation of Nanocrystal Formation and Deformation Behavior of Ti3Al Alloy," *Computational Materials Science,* vol. 98, pp. 245-251, 2015.

[138] R. Pasinot and E. Savino, "Embedded-atom-method interatomic potential for hcp metals," *Phys Rev B,* vol. 45, pp. 12704-12714, 1992.

[139] L. Byeong-Joo, K. Won-Seok, K. Hyun-Kyu and K. Eun-Ha, "The modified embedded-atom method interatomic potentials and recent progress in atomistic simulations," *Calphad,* vol. 34, no. 4, pp. 510-522, 2010.

[140] N. Chen, "Mobius Inversion in physics," World Scientific, Singapore, 2010.